

Block Based Deconvolution Algorithm Using Spline Wavelet Packets

Amir Averbuch · Valery Zheludev ·
Pekka Neittaanmäki · Jenny Koren

Published online: 3 September 2010
© Springer Science+Business Media, LLC 2010

Abstract This paper presents robust algorithms to deconvolve discrete noised signals and images. The idea behind the algorithms is to solve the convolution equation separately in different frequency bands. This is achieved by using spline wavelet packets. The solutions are derived as linear combinations of the wavelet packets that minimize some parameterized quadratic functionals. Parameters choice, which is performed automatically, determines the trade-off between the solution regularity and the initial data approximation. This technique, which is called Spline Harmonic Analysis, provides a unified computational scheme for the design of orthonormal spline wavelet packets, fast implementation of the algorithm and an explicit representation of the solutions. The presented algorithms provide stable solutions that accurately approximate the original objects.

Keywords Deconvolution · Wavelet packet · Spline · Regularity

1 Introduction

Deconvolution is a required operation in many signal processing applications such as system identification, spectroscopy, seismic processing, image deblurring, to name a few. This is an active area of research with many publications. No universal algorithm has been developed so far.

The reason lies in a diversity of applications and in the intrinsic ill-posedness of the problem. The ill-posedness of the problem stems from the fact that a direct convolution of a signal (in applications, convolution means, for example, measuring a signal by an instrument, transmission through a channel, propagation of a seismic signal through the earth, observation of a distant or small object through an optical device) results in smoothing. Measurements of the convolved signal are typically available in a discrete set of points and comprise errors. Thus, a straightforward inversion of the convolution operator leads to an amplification of these errors. Therefore, this inversion is far from being stable and robust. A number of approaches have been suggested to overcome this instability starting from the classical work by Wiener [27]. Recently, wavelet based methods [6, 7, 14] were presented. However, by now, the most efficient deconvolution algorithms are based on Tikhonov regularization method [22, 23] and related schemes [16, 20]. Non-quadratic constraints, which result in sparse solutions are investigated in [11]. Wavelets and regularization methods that are based on Fourier transform, were combined in [10, 12, 19, 24].

Naturally, in problems where convolution is involved, Fourier transform is widely used. However, in signal processing applications, some contradiction exists between continuous convolution, which physical devices produce, and the discreteness of the processed data. Spline functions enable to overcome this contradiction by mapping the discrete data into spaces of smooth functions. An additional advantage of using splines for deconvolution applications lies in their abilities to effectively control the smoothness of the solution. The Spline Harmonic Analysis (SHA) technique, which was developed in [29, 31, 32], combines the splines approximation abilities with the computational strength of the Fast Fourier transform. The SHA perfectly matches the so-

A. Averbuch (✉) · V. Zheludev · J. Koren
School of Computer Science, Tel Aviv University, Tel Aviv
69978, Israel
e-mail: amir@math.tau.ac.il

P. Neittaanmäki
Department of Mathematical Information Technology, University
of Jyväskylä, P.O. Box 35 (Agora), Jyväskylä, Finland

lution of convolution-related problems. In addition, SHA appears useful for the construction of wavelet transforms in spline spaces [1, 32]. A non-periodic version of this harmonic analysis was presented in [33, 34].

A fast spline-based algorithm for solving the convolution integral equation, which is based on Tikhonov regularization, was presented in [2]. According to Tikhonov regularization methodology, the approximated solution is derived as a minimizer of a parameterized functional consisting of two components. One is the discrepancy functional, which measures the approximation of the available data. The other is the stabilizer, which controls the regularity of the solution. The numerical regularization parameter provides a trade-off between the approximation and the regularity. This parameter is derived automatically. Its value depends on the relative shares of the coherent signal and the noise in the available data.

The relative parts of the coherent signal and the noise in different frequency components of the data are different. To take this into account, we propose to solve the convolution equation separately in different frequency bands, while the regularization parameters are to be found according to the signal-to-noise ratio in each band. This approach significantly extends the adaptation abilities and the robustness of the method. Practically, this scheme is implemented via the application of the orthonormal spline wavelet packets. These wavelet packets, which are constructed by using the SHA, provide a split of the frequency domain of a signal or an image into a set of bands whose overlap is minimal. The Best Basis methodology [8, 26] enables to find an optimal partition of the frequency domain for the given signal or image. The SHA provides a unified convolution-tailored computational framework for the design of wavelet packets, selection of the Best Basis, fast implementation of the solution and automatic choices of the parameters in different wavelet packet subspaces. Another method to select essential frequency bands is presented as the Block Pursuit algorithm (BPA). This method, which, to some extent, is related to the Matching Pursuit [18], enables, in several cases, to achieve a superior restoration quality at the expense of much higher computational cost compared to the Best Basis scheme. The solutions are explicitly represented by splines. Their values at integer grid points are calculated by application of the inverse fast Fourier transform (FFT), while the values at diadic or triadic rational points can be calculated by using fast subdivision algorithms [35, 36].

Together with the general problem of restoration of the signal (image), which was subjected to convolution and corrupted by noise, the presented algorithm efficiently handles two extreme cases: pure deconvolution when noise is not present and denoising when convolution is not used.

The paper is organized as follows. In Sect. 2, we formulate the problems to be solved and provide some needed

facts about periodic splines and outline the SHA. The standard Tikhonov scheme of an approximated solution of the convolution equation in one and two dimensions is described in Sect. 3. In Sect. 4, we construct the spline wavelet packets. The algorithms for solution of the one-dimensional convolution equation in separate wavelet packet subspaces is given in Sect. 5. Section 6 does the same for the two-dimensional convolution equation. Numerical results from the experiments on deconvolution and denoising of images are given in Sect. 7.

2 Preliminaries

2.1 Notation and Formulation of the Problems

The one-dimensional convolution equation is $g(x) = \int_{-\infty}^{\infty} h(x-s)f(s)ds$. Here f is an unknown sought after function, h is the kernel and g is the given data function. Typically in applications, the functions h and the unknown function f are compactly supported then, necessarily, g has a compact support as well. Then, the deconvolution problem can be reduced to finding an N -periodic solution of the equation

$$g(x) = h(x) \star f(x) = \int_0^N h(x-y)f(y)dy, \quad (2.1)$$

where the unknown function $f(x)$, the blurring kernel $h(x)$ and the data function $g(x)$ are N -periodic. If $h(x) \in C^l$ and $f(x) \in C^m$ then $g(x) \in C^{l+m+1}$.

In most practical situations, the available data is being sampled on the grid $\{x_k\}$. These samples are corrupted by a random noise $\mathbf{e} = \{e_k\}$. Then, only approximated solutions are possible. We assume that the grid is uniform $\{x_k = k\}$. Let $N = 2^j$ ($j \in \mathbb{N}$) be the number of nodes on the grid. Denote $\mathbf{g} = \{g(k)\}_{k=0}^{N-1}$, $\mathbf{h} = \{h(k)\}_{k=0}^{N-1}$ and $\mathbf{z} = \mathbf{g} + \mathbf{e}$. The two-dimensional periodic convolution equation is defined as

$$g(x, y) = h(x, y) \star f(x, y) \\ \triangleq \int_0^N \int_0^N h(x-s, y-t)f(s, t)dsdt, \quad (2.2)$$

where the unknown function $f(x, y)$, the blurring kernel $h(x, y)$ and the data function $g(x, y)$ are N -periodic. In two-dimensional case, the term *periodic* means N -periodicity in both directions.

We assume that the kernel h and the data function g have continuous derivatives in both directions. We assume that the data is sampled on the grid $\{(k, n)\}$. The samples are corrupted by a random noise $\mathbf{e} = \{e_{k,n}\}$. In addition, we assume that only samples from the periodic kernel h on the grid $\{(k, n)\}$ are known. Thus, we have at our disposal N -periodic arrays \mathbf{z} and \mathbf{h} such that $\mathbf{z} = \{z_{k,n}\} = \{g(k, n) + e_{k,n}\}$, $\mathbf{h} \triangleq \{h(k, n)\}$ and $k, n = 0, \dots, N-1$.

In the sequel the following notation will be used. $\omega \triangleq e^{2\pi i/N}$. The Discrete Fourier Transform (DFT) of a vector $\mathbf{a} \triangleq \{a_k\}_{k=0}^{N-1}$ and its inverse (IDFT) are $\hat{a}(n) \triangleq \sum_{k=0}^{N-1} \omega^{-nk} a_k$, and $a_k = N^{-1} \sum_{n=0}^{N-1} \omega^{nk} \hat{a}(n)$, respectively. The circular discrete convolution $\mathbf{c} \triangleq \{c_k\}_{k=0}^{N-1}$ of N -periodic signals $\mathbf{a} \triangleq \{a_k\}$ and $\mathbf{b} \triangleq \{b_k\}$ is $\mathbf{c} = \mathbf{a} * \mathbf{b} \iff c_k = \sum_{l=0}^{N-1} a_{k-l} b_l$. Then, the DFT of the convolution is $\hat{c}(n) = \hat{a}(n) \hat{b}(n)$.

The 2D direct and inverse DFTs of an array $\mathbf{a} \triangleq \{a_{k,n}\}$ are $\hat{a}(\kappa, \nu) \triangleq \sum_{k,n=0}^{N-1} \omega^{-k\kappa-n\nu} a_{k,n}$, $a_{k,n} = N^{-2} \times \sum_{\kappa,\nu=0}^{N-1} \omega^{k\kappa+n\nu} \hat{a}(\kappa, \nu)$, respectively. The circular discrete convolution $\mathbf{c} \triangleq \{c_{k,n}\}$ of periodic arrays \mathbf{a} and $\mathbf{b} \triangleq \{b_{k,n}\}$ and its DFT are linked by $\mathbf{c} = \mathbf{a} * \mathbf{b} \iff c_{k,n} = \sum_{l,m=0}^{N-1} a_{k-l,n-m} b_{l,m} \iff \hat{c}(\kappa, \nu) = \hat{a}(\kappa, \nu) \hat{b}(\kappa, \nu)$.

We propose to find the approximated solutions of (2.1) and (2.2) as linear combinations of 1D and 2D periodic spline wavelet packets, respectively. For this, we utilized the Spline Harmonic Analysis (SHA), which provides an explicit construction of wavelet packets with a fast implementation of the algorithm.

2.2 Outline of SHA

The core of the SHA technique is the introduction of special orthogonal bases in periodic spline spaces. The elements of the basis of the space of N -periodic splines of order p are called the exponential splines (ES). They are the counterparts of the Fourier exponential functions (FEF) and their properties are similar to the properties of the FEF. In particular,

1. The ES are orthogonal to each other;
2. The ES interpolate the FEF;
3. The convolution of two ES is a ES;
4. The integer shift of a ES results in its multiplication by a FEF;
5. A derivative of a ES is a ES.

These properties lead to significant operational advantages once splines are represented via the ES bases. In particular,

1. The ES coordinates of a spline are calculated via the FFT;
2. The Parseval identities for splines and their derivatives hold;
3. Continuous and sampled convolutions of two splines are reduced to multiplication of their coordinates;
4. Interpolation of the grid data is explicit;
5. When convolution equations are solved, all the calculations are reduced to simple operations in the coordinates domain. Return to the spline domain is implemented by the application of the inverse FFT;

6. Introduction of the ES enables explicit construction of the spline wavelet packets that facilitates operations with them.

2.2.1 Periodic Splines

The centered B-splines of the first order on the grid $\{k\}$ is

$$\tilde{B}^1(x) \triangleq \begin{cases} 1, & x \in [-1/2, 1/2], \\ 0, & \text{otherwise.} \end{cases}$$

The periodization of the spline $B^1(x) \triangleq \sum_{l \in \mathbb{Z}} \tilde{B}^1(x + lN)$ is called the N -periodic B-spline of the first order on the grid $\{k\}$. The Fourier expansion of the B-spline is:

$$B^1(x) = \frac{1}{N} \sum_{n=-\infty}^{\infty} C_n(B^1) e^{2\pi i n x / N},$$

$$C_n(B^1) \triangleq \int_0^N e^{-2\pi i n x / N} B^1(x) dx = \frac{\sin(\pi n / N)}{\pi n / N}.$$

The periodic B-spline of order p is defined via the iterated circular convolution $B^p(x) \triangleq B^1(x) \star B^{p-1}(x)$. Respectively, its Fourier coefficients are

$$C_n(B^p) = (C_n(B^1))^p \\ \iff B^p(x) = \frac{1}{N} \sum_{n=-\infty}^{\infty} \left(\frac{\sin(\pi n / N)}{\pi n / N} \right)^p e^{2\pi i n x / N}.$$

The B-spline $B^p(x)$ is symmetric about zero and non-negative. Its support (up to periodization) is $(-p/2, p/2)$. The spline $B^p(x)$ consists of pieces of polynomials of degree $p - 1$ that are linked to each other at the nodes $\{(k + p/2)\}$ such that $B^p(x)$ belongs to the space C^{p-2} .

Throughout the paper, we assume that the splines are of even order. Thus, the nodes coincide with the grid points. The definition of $B^p(x)$ implies that

$$B^p \star B^m(x) = B^{p+m}(x) \in C^{p+m-2}. \tag{2.3}$$

Translations of B-spline $B^p(x)$ form a basis in the space of N -periodic splines of order p , which have nodes on the grid $\{k\}$. We denote this space by ${}^p\mathcal{S}$. A spline $S^p(x) \in {}^p\mathcal{S}$ and its Fourier coefficients are

$$S^p(x) = \sum_{k=0}^{N-1} q_k B^p(x - k), \tag{2.4}$$

$$C_n(S^p) = \hat{q}(n) C_n(B^p) = \hat{q}(n) \left(\frac{\sin(\pi n / N)}{\pi n / N} \right)^p,$$

$$\hat{q}(n) \triangleq \sum_{k=0}^{N-1} \omega^{-kn} q_k, \quad q_k = \frac{1}{N} \sum_{n=0}^{N-1} \omega^{kn} \hat{q}(n), \tag{2.5}$$

$$k, n = 0, 1, \dots, N - 1.$$

It follows from (2.3) that the convolution of two periodic splines

$$S_1^p \star S_2^m(x) = S_3^{p+m}(x) \in {}^{p+m}\mathcal{S} \subset C^{p+m-2} \tag{2.6}$$

is a spline, whose order is equal to the sum of the orders of the convolved splines.

2.2.2 Exponential Splines

There exist orthogonal (in the Hilbert space $L^2[0, N]$ sense) bases in the spaces ${}^p\mathcal{S}$ of periodic splines, which resemble the Fourier basis of the space of periodic functions that consist of complex exponential functions. From now on, when there is no confusion, the order p indicator will be omitted. Therefore, the notation $S(x) \in {}^p\mathcal{S}$ means that it is the N -periodic spline of order p on the grid $\{k\}$.

Assume that a spline $S(x) \in {}^p\mathcal{S}$ is represented as in (2.4). After substituting (2.5) into (2.4), we get

$$\begin{aligned} S(x) &= \sum_{k=0}^{N-1} B(x-k) \frac{1}{N} \sum_{n=0}^{N-1} \omega^{nk} \hat{q}(n) \\ &= \frac{1}{N} \sum_{n=0}^{N-1} \xi_n \beta_n(x), \end{aligned} \tag{2.7}$$

where the exponential splines $\beta_n^p(x)$ are defined as

$$\beta_n^p(x) \triangleq \sum_{k=0}^N \omega^{nk} B^p(x-k) = \sum_{k=0}^{N-1} \omega^{-nk} B^p(x+k) \tag{2.8}$$

and the coordinates are $\xi_n = \hat{q}(n)$.

The functions $\beta_n(x)$ are the N -periodic splines from the space ${}^p\mathcal{S}$, whose coefficients in the B-spline basis are $\{\omega^{nk}\}$. The spline sequence $\{\beta_n(x)\}$ is N -periodic with respect to n . Thus, the spline $\beta_n(x)$ can be interpreted as a periodic version of the Zak Transform [15, 28] of the B-spline $B(x)$. The non-periodic exponential splines were introduced by Schoenberg [21, p. 17].

The Fourier coefficients of exponential splines are calculated by using (2.4) and (2.8):

$$\begin{aligned} C_m(\beta_n^p) &= C_m(B^p) \sum_{k=0}^{N-1} \omega^{k(m-n)} \\ &= N \delta_m^n \pmod{N} \left(\frac{\sin(\pi m/N)}{\pi m/N} \right)^p, \end{aligned} \tag{2.9}$$

where δ_m^n is the Kronecker delta. Then, the Fourier series expansion of $\beta_n^p(x)$ is:

$$\beta_n^p(x) = \frac{1}{N} \sum_{m=-\infty}^{\infty} e^{2\pi i m x/N} C_m(\beta_n^p)$$

$$\begin{aligned} &= \sum_{m=-\infty}^{\infty} e^{2\pi i(n/N+m)x} \left(\frac{\sin \pi(n/N+m)}{\pi(n/N+m)} \right)^p \\ &= (\sin(\pi n/N))^p \sum_{m=-\infty}^{\infty} \omega^{(n+mN)x} \left(\frac{1}{\pi(n/N+m)} \right)^p. \end{aligned} \tag{2.10}$$

For further use, we single out the sequence

$$\begin{aligned} u_n^p \triangleq \beta_n^p(0) &= \sum_{k=0}^{N-1} \omega^{-nk} B^p(k) \\ &= \sin^p(\pi n/N) \sum_{m=-\infty}^{\infty} \left(\frac{1}{\pi(n/N+m)} \right)^p \\ &= \frac{\sin^p(\pi n/N)}{(\pi(n/N))^p} + O(n^{-p}), \end{aligned} \tag{2.11}$$

which can be explicitly calculated by applying the DFT to the B-splines samples.

The sequences u_n^p are N -periodic and strictly positive. They are symmetric about $N/2$ where they attain their minimum. Their maxima, which are equal to 1, are attained at $\{kN\}_{k=-\infty}^{\infty}$.

2.2.3 Properties of Exponential Splines

We list some properties of exponential splines, which are needed for the spline wavelet packets construction and for the deconvolution algorithm implementation.

Orthogonality: The exponential splines $\{\beta_n^p\}_{n=0}^{N-1}$ form an orthogonal basis for the space ${}^p\mathcal{S}$.

Proof Equation (2.7) implies that the set $\{\beta_n^p\}_{n=0}^{N-1}$ forms a basis for the space ${}^p\mathcal{S}$. It follows from (2.9) and from the Parseval’s identity that the inner product of $\beta_n^p \in {}^p\mathcal{S}$ and $\beta_l^q \in {}^q\mathcal{S}$

$$\begin{aligned} \langle \beta_n^p, \beta_l^q \rangle &= \int_0^N \beta_n^p(x) \overline{\beta_l^q(x)} dx \\ &= \frac{1}{N} \sum_{m=-\infty}^{\infty} C_m(\beta_n^p) \overline{C_m(\beta_l^q)} \\ &= \delta_l^n N (\sin(\pi n/N))^{p+q} \\ &\quad \times \sum_{m=-\infty}^{\infty} \left(\frac{1}{\pi(n/N+m)} \right)^{p+q} \\ &= \delta_l^n N u_n^{p+q}, \end{aligned} \tag{2.12}$$

$$\langle \beta_n^p, \beta_l^p \rangle = \delta_l^n N u_n^{2p}, \quad \|\beta_n^p\|^2 = N u_n^{2p}. \tag{2.13}$$

□

Derivatives:

$$\begin{aligned}
 & \langle (\beta_n^p)^{(s)}, (\beta_l^q)^{(s)} \rangle \\
 &= \frac{1}{N} \sum_{m=-\infty}^{\infty} (2\pi m/N)^{2s} C_m(\beta_n^p) \overline{C_m(\beta_l^q)} \\
 &= \delta_l^n N (2 \sin(\pi n/N))^{2s} (\sin(\pi n/N))^{p+q-2s} \\
 &\quad \times \sum_{m=-\infty}^{\infty} \left(\frac{1}{\pi(n/N+m)} \right)^{p+q-2s} \\
 &= \delta_l^n N (w_n^r)^{2s} u_n^{p+q-2s} \implies \\
 & \|(\beta_n^p)^{(s)}\|^2 = N (w_n)^{2s} u_n^{2p-2s}, \quad w_n \triangleq 2 \sin \frac{\pi n}{N}. \quad (2.14)
 \end{aligned}$$

Shift: The exponential splines are the eigenvectors of the shift operator.

Proof For all $d \in \mathbb{Z}$

$$\beta_n(x+d) = \sum_k^{j-r} \omega^{-nk} B^r(x+(d+k)) = \omega^{nd} \beta_n(x). \quad (2.15)$$

□

Convolution: The convolution of two exponential splines is an exponential spline:

$$\beta_n^p \star \beta_l^q = N \delta_n^l \beta_n^{p+q}. \quad (2.16)$$

Proof If $f(x)$ and $h(x)$ are N -periodic functions and $g(x) = f(x) \star h(x)$ then $C(g)(r) = C(f)(r) \cdot C(h)(r)$. This property together with (2.9) imply (2.16). □

Interpolation: Exponential splines interpolate exponential functions at grid points.

Proof From (2.18), we get $\beta_n^p(k) = \omega^{nk} \beta_n^p(0) \implies \beta_n^p(k)/u_n^p = e^{2\pi i nk/N}$. This property highlights the relationship between exponential functions and exponential splines. □

Orthonormal bases: By normalizing the exponential splines $\{\beta_n^p\}$, we obtain the orthonormal basis $\{\gamma_n^p\}$ of ${}^p\mathcal{S}$. Equation (2.13) implies

$$\gamma_n^p(x) \triangleq \sqrt{\frac{1}{N u_n^{2p}}} \beta_n^p(x), \quad (2.17)$$

$$\|(\gamma_n^p)^{(s)}\|^2 = W_n^{p,s} \triangleq \frac{u_n^{2(p-s)}}{u_n^{2p}} \left(2 \sin \frac{\pi n}{N} \right)^{2s}.$$

The following relations exist

$$\gamma_n(x+d) = \omega^{nd} \gamma_n(x), \quad (2.18)$$

$$\begin{aligned}
 \gamma_n^p \star \gamma_l^q &= \sqrt{N} U_n^{p,q} \delta_n^l \gamma_n^{p+q}, \\
 U_n^{p,q} &\triangleq \sqrt{\frac{u_n^{2(p+q)}}{u_n^{2p} u_n^{2q}}} \quad (2.19)
 \end{aligned}$$

$$\begin{aligned}
 \frac{\sqrt{N} u_n^{2p}}{u_n^p} \gamma_n^p(k) &= e^{2\pi i nk/N} \iff \gamma_n^p(k) = \frac{w^{nk}}{\sqrt{N}} V_n^p, \\
 V_n^p &\triangleq \frac{u_n^p}{\sqrt{u_n^{2p}}}. \quad (2.20)
 \end{aligned}$$

2.2.4 Representation of Periodic Splines by Exponential Splines Basis

Equations (2.7) and (2.17) imply that the expansion of any spline $S^p \in {}^p\mathcal{S}$ via the orthonormal exponential spline basis is

$$\begin{aligned}
 S^p(x) &= \sum_{k=0}^{N-1} q_k B^p(x-k) \\
 &= \sqrt{\frac{1}{N}} \sum_{n=0}^{N-1} \sigma_n \gamma_n^p(x), \quad \sigma_n = \sqrt{u_n^{2p}} \hat{q}(n). \quad (2.21)
 \end{aligned}$$

This expansion imposes a specific form of harmonic analysis methodology onto the spline space, where the exponential splines $\{\gamma_n^p(x)\}_{n=0}^{N-1}$ act as harmonics and the coordinates $\{\sigma_n\}$, $n = 0, \dots, N-1$, which we refer to as the SHA-spectrum of the spline $S^p(x)$, act as the Fourier coefficients. Originally, this construction, which is called SHA, was presented in its final form in [32] but some of its components were exposed in [29, 30]. The usage of SHA significantly simplifies many operations on splines. We describe some of these operations.

Parseval identity: From (2.17), we get:

$$\begin{aligned}
 \|S^p\|^2 &= \frac{1}{N} \sum_{n=0}^{N-1} |\sigma_n|^2, \\
 \|(S^p)^{(s)}\|^2 &= \frac{1}{N} \sum_{n=0}^{N-1} |\sigma_n|^2 W_n^{p,s}. \quad (2.22)
 \end{aligned}$$

Convolution: Let $S^p \in {}^p\mathcal{S}$ be represented as in (2.21) and $S^q(x) = N^{-1/2} \sum_{l=0}^{N-1} \eta_l \gamma_l^q(x) \in {}^q\mathcal{S}$. From (2.19), we have

$$\begin{aligned}
 S^p \star S^q(x) &= \sum_{n,l=0}^{N-1} \sigma_n \eta_l \gamma_n^p \star \gamma_l^q(x) \\
 &= \sqrt{\frac{1}{N}} \sum_{n=0}^{N-1} U_n^{p,q} \sigma_n \eta_n \gamma_n^{p+q}(x) \in {}^{p+q}\mathcal{S}. \quad (2.23)
 \end{aligned}$$

Interpolation: Assume the spline $S^p(x)$ interpolates the data $\{z_k\}$ on the grid $\{k\}$. Then, by using (2.20), we get:

$$\begin{aligned}
 S^p(k) &= \sqrt{\frac{1}{N}} \sum_{n=0}^{N-1} \sigma_n \gamma_n^p(k) \\
 &= \frac{1}{N} \sum_{n=0}^{N-1} \sigma_n V_n^p \omega^{kn} = z_k \iff \sigma_n = \frac{\hat{z}(n)}{V_n^p}.
 \end{aligned}
 \tag{2.24}$$

Hence, the discrete Parseval identity follows:

$$\begin{aligned}
 \sum_{k=0}^{N-1} |S^p(k)|^2 &= \frac{1}{N} \sum_{n=0}^{N-1} |\sigma_n V_n^p|^2 \\
 &= \frac{1}{N} \sum_{n=0}^{N-1} |\sigma_n|^2 \frac{(u_n^p)^2}{u_n^{2p}}.
 \end{aligned}
 \tag{2.25}$$

Remark 2.1 If a spline $S^p(x) \in {}^p\mathcal{S}$ is represented as $S(x) = \sum_{n=0}^{N-1} \sigma_n \gamma_n^p(x)$, then its values at the grid points $\{k\}$, which are given in (2.24), are calculated by the inverse DFT. The values at the dyadic $\{2^{-r}k\}$ or the triadic $\{3^{-r}k\}$ rational points are calculated using fast simple subdivision algorithms [35, 36].

Sampled convolution: By combining (2.23) and (2.24), we get the grid samples of the convolution of two splines.

$$\begin{aligned}
 S^p \star S^q(k) &= \frac{1}{N} \sum_{n=0}^{N-1} \omega^{kn} Q_n^{p,q} \sigma_n \eta_n, \\
 Q_n^{p,q} &\triangleq U_n^{p,q} V_n^{p+q} = \frac{u_n^{p+q}}{\sqrt{u_n^{2p} u_n^{2q}}}.
 \end{aligned}
 \tag{2.26}$$

2.2.5 Exponential Splines—2D Case

The 2D B-spline is defined as a product of 1D B-splines $B^{p,q}(x, y) \triangleq B^p(x)B^q(y)$. Similarly, we can define the N -periodic 2D normalized exponential splines $\gamma_{\kappa,v}^{p,q}(x, y) \triangleq \gamma_{\kappa}^p(x)\gamma_v^q(y)$. 2D splines are defined as linear combinations of the 2D basis splines

$$\begin{aligned}
 S^{p,q}(x, y) &\triangleq \sum_{k,n=0}^{N-1} s_{k,n} B^p(x-k)B^q(y-n) \\
 &= \frac{1}{N} \sum_{\kappa,v} \sigma_{\kappa,v} \gamma_{\kappa,v}^{p,q}(x, y),
 \end{aligned}
 \tag{2.27}$$

$$\begin{aligned}
 \sigma_{\kappa,v} &= \hat{s}(\kappa, v) \sqrt{u_{\kappa}^{2p} u_v^{2q}}, \\
 \hat{s}(\kappa, v) &\triangleq \sum_{k,n=0}^{N-1} \omega^{-k\kappa-nv} s_{k,n}, \\
 s_{k,n} &= \frac{1}{N^2} \sum_{\kappa,v} \omega^{k\kappa+nv} \frac{\sigma_{\kappa,v}}{\sqrt{u_{\kappa}^{2p} u_v^{2q}}}.
 \end{aligned}$$

The spaces of 2D splines $S^{p,q}(x, y)$ are denoted by ${}^{p,q}\mathcal{S}$. The splines $\gamma_{\kappa,v}^{p,q}(x, y)$ form an orthogonal basis of ${}^{p,q}\mathcal{S}$ and the coordinates $\{\sigma_{\kappa,v}\}$ of a spline $S^{p,q}(x, y)$ in this basis are called its 2D SHA spectrum. Extension of the SHA to 2D spline spaces is straightforward. In particular,

Parseval identities:

$$\| (S^{p,q})_{x,y}^{(s,t)} \|^2 = \frac{1}{N^2} \sum_{\kappa,v} W_{\kappa}^{p,s} W_v^{q,t} |\sigma_{\kappa,v}|^2,
 \tag{2.28}$$

where $W_n^{p,s}$ is defined in (2.17).

Convolution: Let

$$S^{\tilde{p},\tilde{q}}(x, y) = \frac{1}{N} \sum_{\kappa,v} \mu_{\kappa,v} \gamma_{\kappa,v}^{\tilde{p},\tilde{q}}(x, y) \in \tilde{p},\tilde{q}\mathcal{S}.
 \tag{2.29}$$

Then the convolution

$$\begin{aligned}
 S^{p,q} \star S^{\tilde{p},\tilde{q}}(x, y) &= \frac{1}{N} \sum_{\kappa,v} \sigma_{\kappa,v} \mu_{\kappa,v} U_{\kappa}^{p,\tilde{p}} U_v^{q,\tilde{q}} \gamma_{\kappa,v}^{(p+\tilde{p}), (q+\tilde{q})}(x, y) \\
 &\in {}^{(p+\tilde{p}), (q+\tilde{q})}\mathcal{S}, \\
 S^{p,q} \star S^{\tilde{p},\tilde{q}}(k, n) &= \frac{1}{N^2} \sum_{\kappa,v} \omega^{(k\kappa+nv)} \sigma_{\kappa,v} \mu_{\kappa,v} Q_{\kappa}^{p,\tilde{p}} Q_v^{q,\tilde{q}}
 \end{aligned}
 \tag{2.30}$$

where $U_n^{p,q}$ and $Q_n^{p,q}$ are defined in (2.23) and (2.26), respectively.

3 Regularized Spline Solution to the Convolution Equation (Tikhonov Solution)

In this section, we briefly outline a scheme, which is based on Tikhonov regularization, of a spline approximation to the solution of (2.1). This scheme is presented in full details in [2]. In addition, the convergence of the approximated solution to the exact one is analyzed in [2].

3.1 One-dimensional Case

In this section, we operate in the spline space ${}^p\mathcal{S}$. Given a sampled data array $\mathbf{z} = \{z_k\}$ and a kernel data array $\mathbf{h} = \{h(k)\}$, we construct the interpolatory spline $\chi(x) = N^{-1/2} \sum_{n=0}^{N-1} \mu_n \gamma_n^q(x) \in {}^q\mathcal{S}$, $\mu_n = \hat{h}(n)/V_n^q$, which interpolates the kernel $h(x)$ on the grid $\{k\}$.

The solution to (2.1) is approximated by the spline from ${}^p\mathcal{S}$. Define the functional on the space ${}^p\mathcal{S}$ to be $J_\rho(S) \triangleq \rho I(S) + E(S)$, where $I(S) \triangleq \|S'\|^2$, $E(S) \triangleq \sum_{i=0}^{N-1} (\chi \star S(i) - z_i)^2$ and ρ is a numerical parameter. If the spline $S(x) \in {}^p\mathcal{S}$ is represented as in (2.21) then, due to (2.22) and (2.26),

$$I(S) = \frac{1}{N} \sum_{n=0}^{N-1} |\sigma_n|^2 W_n^{p,1},$$

$$E(S) = \frac{1}{N} \sum_{n=0}^{N-1} |\sigma_n \mu_n Q_n^{p,q} - \hat{z}(n)|^2. \tag{3.1}$$

Hence, it follows that the spline

$$S_\rho^p(x) = \sqrt{\frac{1}{N}} \sum_{n=0}^{N-1} \sigma_n(\rho) \gamma_n^p(x),$$

$$\sigma_n(\rho) = \frac{\bar{\mu}_n \hat{z}(n) Q_n^{p,q}}{A_n(\rho)}, \quad \text{where}$$

$$A_n(\rho) \triangleq \rho W_n^{p,1} + (|\mu_n| Q_n^{p,q})^2, \tag{3.2}$$

minimizes the functional $J_\rho(S)$.

Assume we are able to estimate the variance $\text{var}(\mathbf{e}) = \varepsilon^2$ of the error vector. The regularization parameter ρ is derived from the solution of the following problem.

Problem FRP: Among the splines S_ρ defined in (3.2), find a spline $S_{\rho(\varepsilon)}$ that minimizes the functional $I(S_\rho)$ under the constraint $E(S_\rho)/N \leq \varepsilon^2$.

Loosely speaking, we are looking for the smoothest spline among the splines S_ρ , for which the standard deviation of the vector $\{\chi \star S_\rho(i)\}$ from the data vector \mathbf{z} does not exceed the standard deviation of the vector \mathbf{z} from the exact data vector $\mathbf{g} = \{g(i)\}$.

Denote $e(\rho) \triangleq E(S_\rho)/N$. It can happen that some coordinates μ_n of the interpolatory spline χ are zero. Then, denote by ζ the set of indices for which $\mu_n = 0$. If ζ is not empty then denote $\mu(z) \triangleq N^{-2} \sum_{n \in \zeta} |\hat{z}(n)|^2$. It follows from (3.2) that

$$e(\rho) = \frac{1}{N^2} \sum_{n=0}^{N-1} \left(\frac{\rho W_n^{p,1} |\hat{z}(n)|}{A_n(\rho)} \right)^2$$

$$= \frac{1}{N^2} \sum_{n \notin \zeta} \left(\frac{\rho W_n^{p,1} |\hat{z}(n)|}{A_n(\rho)} \right)^2 + \mu(z).$$

The function $e(\rho)$ grows strictly monotonically while $e(0) = \mu(z)$ and $\lim_{\rho \rightarrow \infty} e(\rho) = N^{-2} \|\mathbf{z}\|^2$.

On the other hand, the function

$$i(\rho) \triangleq I(S_\rho) = \frac{1}{N} \sum_{n \notin \zeta} \frac{W_n^{p,1} |Q_n^{p,q} \mu_n \hat{z}(n)|^2}{(\rho W_n^{p,1} + (|\mu_n| Q_n^{p,q})^2)}$$

decays strictly monotonically while $\lim_{\rho \rightarrow \infty} i(\rho) = 0$.

Hence, it follows that, if $N^{-1} \|\mathbf{z}\| > \varepsilon$ then Problem FRP has a unique solution $S_{\rho(\varepsilon)}(x) \in {}^p\mathcal{S}$, where the value of the parameter $\rho(\varepsilon)$ is derived from the equation

$$\tilde{e}(\rho) \triangleq \frac{1}{N^2} \sum_{n \notin \zeta} \left(\frac{\rho W_n^{p,1} |\hat{z}(n)|}{A_n(\rho)} \right)^2 = \tilde{\varepsilon}^2, \tag{3.3}$$

$$\tilde{\varepsilon}^2 \triangleq \varepsilon^2 - N^{-2} \sum_{n \in \zeta} |z(n)|^2.$$

Note that $\tilde{\varepsilon}^2$ is the variance evaluation of the “filtered” errors vector

$$\tilde{\mathbf{e}} \triangleq \{\tilde{e}_k\}_{k=0}^{N-1}, \quad \tilde{e}_k = \frac{1}{N} \sum_{n \notin \zeta} \omega^{kn} \hat{e}(n). \tag{3.4}$$

3.2 Two-dimensional Case

Assume $\mathbf{z} = \{z_{k,n}\}$ and $\mathbf{h} = \{h(k,n)\}_{k,n=0}^{N-1}$ are available data arrays. For simplicity, from now on, we assume that x and y components of the 2D splines have the same order. Thus, $\gamma_{\kappa,v}^p(x,y)$ will stand for $\gamma^p(x)\gamma^p(y)$ and $S^p(x,y)$ will stand for $S^{p,p}(x,y) \in {}^{p,p}\mathcal{S}$.

Assume that $\chi(x,y) = N^{-1} \sum_{\kappa,v=0}^{N-1} \mu_{\kappa,v} \gamma_{\kappa,v}^q(x,y) \in {}^{q,q}\mathcal{S}$, $\mu_{\kappa,v} = \hat{h}(\kappa,v)/(V_\kappa^q V_v^q)$, is the spline that interpolates the sampled kernel \mathbf{h} .

Like in the 1D case, we approximate the solution of the deconvolution problem by the spline $S_\rho^p(x,y) \in {}^{p,p}\mathcal{S}$, which minimizes the functional $J_\rho(S) \triangleq \rho I(S) + E(S)$, where $I(S) \triangleq \|S'_x\|^2 + \|S'_y\|^2$, $E(S) \triangleq \sum_{k,n=0}^{N-1} (S \star \chi(k,n) - z_{k,n})^2$. By using (2.28)–(2.30), we derive the solution to the minimization problem

$$S_\rho^p(x,y) = \frac{1}{N} \sum_{\kappa,v=0}^{N-1} \sigma_{\kappa,v}(\rho) \gamma_{\kappa,v}^p(x,y),$$

$$\sigma_{\kappa,v}(\rho) = \frac{\bar{\mu}_{\kappa,v} \hat{z}(\kappa,v) Q_\kappa^{p,q} Q_v^{p,q}}{A_{\kappa,v}(\rho)},$$

$$A_{\kappa,v}(\rho) \triangleq \rho D_{\kappa,v} + (|\eta_{\kappa,v}| Q_\kappa^{p,q} Q_v^{p,q})^2,$$

$$D_{\kappa,v} \triangleq W_\kappa^{p,1} + W_v^{p,1}.$$

Selection of the regularization parameter ρ is similar to the 1D case. We derive it from the equation $N^{-2}E({}^pS_\rho) = \varepsilon^2$, where $\varepsilon^2 \triangleq N^{-2} \sum_{k,n} e_{k,n}^2$ is the variance's estimate of the zero-mean error array. This equation is equivalent to

$$\sum_{\kappa, \nu \notin \theta} \left(\frac{\rho D_{\kappa, \nu} |\hat{z}(\kappa, \nu)|}{A_{\kappa, \nu}(\rho)} \right)^2 + \mu(z) = \varepsilon^2,$$

where θ is the set of indices $\{\kappa, \nu\}$ such that $\eta_{\kappa, \nu} = 0$, and $\mu(z) \triangleq \sum_{(\kappa, \nu) \in \theta} |z(\kappa, \nu)|^2$.

Remark The regularization parameter ρ provides a trade-off between the approximation of the available data \mathbf{z} and the regularity of the solution. The value of ρ is determined by the relative contributions of the coherent signal and of the noise into the data \mathbf{z} . These contributions are different in different frequency bands. Therefore, we gain better adaptivity of the algorithm if the values of the parameter ρ are derived differently for different frequency bands. This can be efficiently implemented by introducing the spline wavelet packets.

4 Construction of the Spline Wavelet Packets

We construct wavelet packets using the SHA technique, which was presented in Sect. 2. The wavelet packets to be constructed are symmetric and well localized in both time and frequency domains. Orthogonality relations between groups of wavelet packets exist. In addition, the SHA technique simplifies the operations on these objects, especially convolution operations. The construction is based on the relations between exponential splines from spline spaces of different resolution scales.

4.1 Split of the Spline Space

4.1.1 Spline Spaces of Different Resolution Scales

Denote by ${}^pS^{r,0}$, $r \in \mathbb{N}$, the space of N -periodic splines of even order p on the grid $\{2^r k\}$. This is $N/2^r$ -dimensional space, where a basis consists of shifts of B-splines

$$B_r(x) \triangleq \frac{1}{N} \sum_{n=-\infty}^{\infty} \left(\frac{\sin(2^r \pi n/N)}{2^r \pi n/N} \right)^p e^{2\pi i n x/N}. \tag{4.1}$$

A spline $S(x) \in {}^pS^{r,0}$ can be represented as

$$S(x) = \sum_{k=0}^{N/2^r-1} q_k B_r(x - 2^r k),$$

$$C_n({}^pS^r) = \hat{q}(n) C_n(B_r) = \hat{q}(n) \left(\frac{\sin(2^r \pi n/N)}{2^r \pi n/N} \right)^p$$

$$\begin{aligned} \hat{q}(n) &\triangleq \sum_{k=0}^{N/2^r-1} \omega^{-2^r kn} q_k, \\ q_k &= \frac{2^r}{N} \sum_{n=0}^{N/2^r-1} \omega^{2^r kn} \hat{q}(n), \\ k, n &= 0, 1, \dots, N/2^{N/2^r-1} - 1. \end{aligned}$$

Obviously, a spline, whose nodes are located at the even grid points $\{2k\}$ belongs at the same time to the whole space pS of splines with nodes at $\{k\}$. Thus, ${}^pS^{r,0} \subset {}^pS^{r-1,0} \subset \dots \subset {}^pS^{0,0} \equiv {}^pS$. Similarly to the space pS , we introduce the orthogonal bases of exponential splines in the spaces ${}^pS^{r,0}$:

$$\begin{aligned} {}^p\beta_n^{r,0}(x) &\triangleq \sum_{k=0}^{N/2^r-1} \omega^{2^r nk} B_r(x - 2^r k) \\ &= 2^{-r} \sum_{m=-\infty}^{\infty} e^{2\pi i(n/N+2^{-r}m)x} \\ &\quad \times \left(\frac{\sin \pi(2^r n/N + m)}{\pi(2^r n/N + m)} \right)^p, \end{aligned} \tag{4.2}$$

$${}^p u_n^r \triangleq {}^p\beta_n^{r,0}(0) = 2^{-r} \sum_{m=-\infty}^{\infty} \left(\frac{\sin \pi(2^r n/N + m)}{\pi(2^r n/N + m)} \right)^p. \tag{4.3}$$

A spline $S(x) \in {}^pS^{r,0}$ is represented as

$$S(x) = \frac{2^r}{N} \sum_{n=0}^{N/2^r-1} \xi_n {}^p\beta_n^{r,0}(x), \tag{4.4}$$

and the coordinates $\xi_n = \hat{q}(n)$. The inner products

$$\begin{aligned} \langle {}^p\beta_n^{r,0}, {}^q\beta_l^{r,0} \rangle &= \delta_l^n 2^{-r} N^{p+q} u_n^r \\ \implies \| {}^p\beta_n^{r,0} \|^2 &= 2^{-r} N^{2p} u_n^r. \end{aligned}$$

Thus, the exponential splines, which form an orthonormal basis in the space ${}^pS^{r,0}$, are

$$\begin{aligned} {}^p\gamma_n^{r,0}(x) &\triangleq \sqrt{\frac{2^r}{N^{2p} u_n^r}} {}^p\beta_n^{r,0}(x), \\ S(x) &= \sqrt{\frac{2^r}{N}} \sum_{n=0}^{N/2^r-1} \sigma_n^{r,0} \gamma_n^{r,0}(x), \\ \sigma_n^{r,0} &= \sqrt{2^p u_n^r} \hat{q}(n). \end{aligned} \tag{4.5}$$

Remark 1 For splines on the initial scale ($r = 0$), we retain the previous notation: $\beta_n^p \equiv {}^p\beta_n^{0,0}$, $\gamma_n^p \equiv {}^p\gamma_n^{0,0}$, $u_n^p \equiv {}^p u_n^0$.

4.1.2 Two-scale Relations

The spline space ${}^p\mathcal{S}^{r,0}$ is a subspace of ${}^p\mathcal{S}^{r-1,0}$. Therefore, the basic splines $\{\beta_n^{r,0}(x)\}$ can be expressed via the splines $\{\beta_l^{r-1,0}(x)\}$.

Theorem 4.1 *The two-scale relation*

$$\beta_n^{r,0}(x) = a_n^{r-1,0}\beta_n^{r-1,0}(x) + a_{n+2^{-r}N}^{r-1,0}\beta_{n+2^{-r}N}^{r-1,0}(x) \quad (4.6)$$

where $a_n^{r-1,0} \triangleq 1/2 \cos^p(2^{r-1}\pi n/N)$ holds for $n = 0, 1, \dots, 2^{-r}N - 1$.

Proof From the separation between even and odd terms in the Fourier series in (4.3), we get:

$$\begin{aligned} \beta_n^{r,0}(x) &= \frac{1}{2^r} \sum_{m=-\infty}^{\infty} e^{2\pi i(n/N+2^{-r+1}m)x} \\ &\quad \times \left(\frac{\sin 2\pi(2^{r-1}n/N+m)}{2\pi(2^{r-1}n/N+m)} \right)^p \\ &\quad + \frac{1}{2^r} \sum_{m=-\infty}^{\infty} e^{2\pi i((n+2^{-r}N)/N+2^{-r+1}m)x} \\ &\quad \times \left(\frac{\sin 2\pi(2^{r-1}(n+2^{-r}N)/N+m)}{2\pi(2^{r-1}(n+2^{-r}N)/N+m)} \right)^p \\ &= \frac{(\cos \pi(2^{r-1}n/N))^p}{2^r} \sum_{m=-\infty}^{\infty} e^{2\pi i(n/N+2^{-r+1}m)x} \\ &\quad \times \left(\frac{\sin \pi(2^{r-1}n/N+m)}{\pi(2^{r-1}n/N+m)} \right)^p \\ &\quad + \frac{(\cos \pi(2^{r-1}(n+2^{-r}N)/N))^p}{2^r} \\ &\quad \times \sum_{m=-\infty}^{\infty} e^{2\pi i((n+2^{-r}N)/N+2^{-r+1}m)x} \\ &\quad \times \left(\frac{\sin \pi(2^{r-1}(n+2^{-r}N)/N+m)}{\pi(2^{r-1}(n+2^{-r}N)/N+m)} \right)^p. \end{aligned}$$

Comparison between the last equation and (4.3) yields (4.6). \square

Corollary 1 *The two-scale relation*

$$\begin{aligned} \gamma_n^{r,0}(x) &= b_n^{r-1,0}\gamma_n^{r-1,0}(x) + b_{n+2^{-r}N}^{r-1,0}\gamma_{n+2^{-r}N}^{r-1,0}(x), \\ b_n^{r-1,0} &\triangleq \sqrt{\frac{2^p u_n^{r-1}}{2^{2p} u_n^r}} \cos^p\left(\frac{2^{r-1}\pi n}{N}\right) \end{aligned} \quad (4.7)$$

for the normalized exponential splines holds for $n = 0, 1, \dots, 2^{-r}N - 1$.

The norms of the splines $\gamma_n^{r,0}$ and $\gamma_n^{r-1,0}$ are equal to one. Hence, we have

$$(b_n^{r-1,0})^2 + (b_{n+2^{-r}N}^{r-1,0})^2 = 1, \quad n = 0, 1, \dots, 2^{-r}N - 1. \quad (4.8)$$

Denote by ${}^p\mathcal{S}^{r,1}$ the orthogonal complement to ${}^p\mathcal{S}^{r,0}$ in the space ${}^p\mathcal{S}^{r-1,0}$. We construct an orthonormal basis that characterizes ${}^p\mathcal{S}^{r,1}$. Define the splines

$$\begin{aligned} \gamma_n^{r,1}(x) &= b_n^{r-1,1}\gamma_n^{r-1,0}(x) + b_{n+2^{-r}N}^{r-1,1}\gamma_{n+2^{-r}N}^{r-1,0}(x), \\ b_n^{r-1,1} &\triangleq \omega^{2^{r-1}n} b_{n+2^{-r}N}^{r-1,0} \\ &= \omega^{2^{r-1}n} \sqrt{\frac{2^p u_{n+2^{-r}N}^{r-1}}{2^{2p} u_n^r}} \sin^p\left(\frac{2^{r-1}\pi n}{N}\right) \end{aligned} \quad (4.9)$$

Proposition 4.1 *The set of splines $\{\gamma_n^{r,1}(x)\}_{n=0}^{2^{-r}N-1}$ forms an orthonormal basis for the space ${}^p\mathcal{S}^{r,1}$.*

Proof The orthogonality of the splines $\{\gamma_n^{r-1,0}(x)\}_{n=0}^{N/2^{r-1}-1}$ results in the orthogonality of $\gamma_n^{r,1}(x)$ to each $\gamma_l^{r,0}(x) \in {}^p\mathcal{S}^{r,0}$ and, when $n \neq l$, to $\gamma_l^{r,1}(x) \in {}^p\mathcal{S}^{r,1}$. Due to (4.8), $\|\gamma_n^{r,1}\|^2 = (b_{n+2^{-r}N}^{r-1,0})^2 + (b_n^{r-1,0})^2 = 1$. It remains to establish the orthogonality relation between $\gamma_n^{r,1}(x)$ and $\gamma_n^{r,0}(x)$. From (4.7) and (4.9), we have:

$$\begin{aligned} \langle \gamma_n^{r,1}, \gamma_n^{r,0} \rangle &= b_n^{r-1,1} b_n^{r-1,0} + b_{n+2^{-r}N}^{r-1,1} b_{n+2^{-r}N}^{r-1,0} \\ &= \omega^{2^{r-1}n} (b_{n+2^{-r}N}^{r-1,0} b_n^{r-1,0} - b_{n+2^{-r}N}^{r-1,0} b_n^{r-1,0}) \\ &= 0. \end{aligned} \quad (4.10)$$

\square

Proposition 4.2 *The splines $\gamma_n^{r,l}(x)$ are the eigenvectors of the shift operator*

$$\gamma_n^{r,l}(x + 2^r k) = \omega^{2^r nk} \gamma_n^{r,l}(x), \quad d = 0, \dots, 2^{-r}N - 1. \quad (4.11)$$

Proof At the initial scale, we have from (2.15) that $\gamma_n^{0,0}(x + k) = \omega^{kn} \gamma_n^{0,0}(x)$. At the first scale for $l = 0, 1$

$$\begin{aligned} \gamma_n^{1,l}(x + 2k) &= b_n^{1,l} \gamma_n^{0,0}(x + 2k) + b_{n+N/2}^{1,l} \gamma_{n+N/2}^{0,0}(x + 2k) \\ &= \omega^{2kn} \gamma_n^{1,l}(x). \end{aligned}$$

For $r > 1$, (4.11) is derived by induction. \square

Note that the union $\{\gamma_n^{r,0}(x)\} \cup \{\gamma_n^{r,1}(x)\}$, $n = 0, \dots, 2^{-r}N - 1$, forms an orthonormal basis for the entire space ${}^p\mathcal{S}^{r-1,0}$.

4.1.3 Refined Split of the Spline Space into Orthogonal Subspaces

The spline space ${}^p\mathcal{S}^{r-1,0}$ is split into the orthogonal sum ${}^p\mathcal{S}^{r-1,0} = {}^p\mathcal{S}^{r,0} \oplus {}^p\mathcal{S}^{r,1}$. If $r > 1$, then we can apply a similar procedure to the space ${}^p\mathcal{S}^{r-1,1}$. As a result, we get the decomposition ${}^p\mathcal{S}^{r-1,1} = {}^p\mathcal{S}^{r,2} \oplus {}^p\mathcal{S}^{r,3}$. In general, the space ${}^p\mathcal{S}^{r-1,l}$ is decomposed into the orthogonal sum ${}^p\mathcal{S}^{r-1,l} = {}^p\mathcal{S}^{r,2l} \oplus {}^p\mathcal{S}^{r,2l+1}$ by the following procedure. Assume that the set of splines $\{\gamma_n^{r-1,l}(x)\}_{n=0}^{N/2^{r-1}-1}$ forms an orthonormal basis of the space ${}^p\mathcal{S}^{r-1,l}$. We construct a new orthonormal basis that consists of two different blocks, which are orthogonal to each other, using the coefficients $b_n^{r-1,0}$ and $b_n^{r-1,1}$ defined in (4.7) and (4.9).

Define two sets of orthonormal splines by using the coefficients $b_n^{r-1,l}$ defined in (4.7) and (4.9):

$$\begin{aligned} \gamma_n^{r,2l+m}(x) &= b_n^{r-1,l} \gamma_n^{r-1,l}(x) + b_{n+2^{-r}N}^{r-1,l} \gamma_{n+2^{-r}N}^{r-1,l}(x), \\ m &= 0, 1, n = 0, \dots, 2^{-r}N - 1. \end{aligned}$$

Denote by ${}^p\mathcal{S}^{r,2l}$ and ${}^p\mathcal{S}^{r,2l+1}$ the linear spans of the orthonormal systems $\{\gamma_n^{r,2l}(x)\}_{n=0}^{2^{-r}N-1}$ and $\{\gamma_n^{r,2l+1}(x)\}_{n=0}^{2^{-r}N-1}$, respectively. Their mutual orthogonality is established similarly to Proposition 4.1. Thus, ${}^p\mathcal{S}^{r-1,l} = {}^p\mathcal{S}^{r,2l} \oplus {}^p\mathcal{S}^{r,2l+1}$ and the union $\{\gamma_n^{r,2l}(x)\} \cup \{\gamma_n^{r,2l+1}(x)\}$, $n = 0, \dots, 2^{-r}N - 1$, forms its orthonormal basis.

Consequently, the spline space ${}^p\mathcal{S}$ can be decomposed into a series of orthogonal sums

$$\begin{aligned} {}^p\mathcal{S} &= {}^p\mathcal{S}^{1,0} \oplus {}^p\mathcal{S}^{1,1} = {}^p\mathcal{S}^{2,0} \oplus {}^p\mathcal{S}^{2,1} \oplus {}^p\mathcal{S}^{2,2} \oplus {}^p\mathcal{S}^{2,3} \\ &= \dots = \bigoplus_{l=0}^{2^r-1} {}^p\mathcal{S}^{r,l}. \end{aligned} \tag{4.12}$$

4.2 Transforms of the Spline’s Coordinates

Let a spline $S(x) \in {}^p\mathcal{S}^{r-1,l}$ be represented by

$$\begin{aligned} S(x) &= \sqrt{\frac{2^{r-1}}{N}} \sum_{n=0}^{N/2^{r-1}-1} \sigma_n^{r-1,l} \gamma_n^{r-1,l}(x) \\ &= \sqrt{\frac{2^r}{N}} \sum_{n=0}^{N/2^r-1} \sigma_n^{r,2l} \gamma_n^{r,2l}(x) \\ &\quad + \sqrt{\frac{2^r}{N}} \sum_{n=0}^{N/2^r-1} \sigma_n^{r,2l+1} \gamma_n^{r,2l+1}(x). \end{aligned}$$

Recall that the sums in the right hand side of the above equation are the orthogonal projections of the spline $S(x) \in {}^p\mathcal{S}^{r-1,l}$ onto the mutually orthogonal subspaces ${}^p\mathcal{S}^{r,2l}$ and ${}^p\mathcal{S}^{r,2l+1}$. The inner products for $m = 0, 1$,

$n = 0, 1, \dots, N/2^r - 1$ are

$$\begin{aligned} \langle S, \gamma_n^{r,2l+m} \rangle &= \sqrt{\frac{2^r}{N}} \sigma_n^{r,2l+m} \\ &= \langle S, b_n^{r-1,m} \gamma_n^{r-1,l} + b_{n+2^{-r}N}^{r-1,m} \gamma_{n+2^{-r}N}^{r-1,l} \rangle \\ &= \sqrt{\frac{2^{r-1}}{N}} (b_n^{r-1,m} \sigma_n^{r-1,l} + b_{n+2^{-r}N}^{r-1,m} \sigma_{n+2^{-r}N}^{r-1,l}) \\ &\implies \sigma_n^{r,2l+m} \\ &= \sqrt{\frac{1}{2}} (b_n^{r-1,m} \sigma_n^{r-1,l} + b_{n+2^{-r}N}^{r-1,m} \sigma_{n+2^{-r}N}^{r-1,l}). \end{aligned} \tag{4.13}$$

Denote for $n = 0, 1, \dots, N/2^r - 1$

$$\begin{aligned} \tilde{\mathbf{B}}_n^{r-1} &\triangleq \begin{pmatrix} b_n^{r-1,0} & b_{n+2^{-r}N}^{r-1,0} \\ b_n^{r-1,1} & b_{n+2^{-r}N}^{r-1,1} \end{pmatrix} \\ &= \begin{pmatrix} b_n^{r-1,0} & b_{n+2^{-r}N}^{r-1,0} \\ \omega^{n2^{r-1}} b_{n+2^{-r}N}^{r-1,0} & -\omega^{n2^{r-1}} b_n^{r-1,0} \end{pmatrix}. \end{aligned} \tag{4.14}$$

Then, we can rewrite (4.13) as

$$\begin{pmatrix} \sigma_n^{r,2l} \\ \sigma_n^{r,2l+1} \end{pmatrix} = \sqrt{\frac{1}{2}} \tilde{\mathbf{B}}_n^{r-1} \cdot \begin{pmatrix} \sigma_n^{r-1,l} \\ \sigma_{n+2^{-r}N}^{r-1,l} \end{pmatrix}. \tag{4.15}$$

Equations (4.8), (4.9) and (4.10) imply that the matrices $\tilde{\mathbf{B}}_n^{r-1}$ are unitary and the inverse matrices

$$\begin{aligned} \mathbf{B}_n^{r-1} &\triangleq (\tilde{\mathbf{B}}_n^{r-1})^{-1} = (\tilde{\mathbf{B}}_n^{r-1})^* \\ &= \begin{pmatrix} b_n^{r-1,0} & \omega^{-n2^{r-1}} b_{n+2^{-r}N}^{r-1,0} \\ b_{n+2^{-r}N}^{r-1,0} & -\omega^{-n2^{r-1}} b_n^{r-1,0} \end{pmatrix} \\ &= \begin{pmatrix} b_n^{r-1,0} & \omega^{-n2^r} b_{n+2^{-r}N}^{r-1,1} \\ b_{n+2^{-r}N}^{r-1,0} & -\omega^{-n2^r} b_{n+2^{-r}N}^{r-1,1} \end{pmatrix}. \end{aligned}$$

Hence, the inverse transform is

$$\begin{aligned} \begin{pmatrix} \sigma_n^{r-1,l} \\ \sigma_{n+2^{-r}N}^{r-1,l} \end{pmatrix} &= \sqrt{2} \mathbf{B}_n^{r-1} \cdot \begin{pmatrix} \sigma_n^{r,2l} \\ \sigma_n^{r,2l+1} \end{pmatrix}, \\ n &= 0, \dots, 2^{-r}N - 1, \\ \iff \sigma_n^{r-1,l} &= \sqrt{2} (b_n^{r-1,0} \sigma_n^{r,2l} + \omega^{-n2^r} b_{n+2^{-r}N}^{r-1,1} \sigma_n^{r,2l+1}), \\ n &= 0, \dots, 2^{-r+1}N - 1. \end{aligned} \tag{4.16}$$

Starting from $r = 0$, subsequent iteration of the relation (4.15) provides the coordinates for the orthogonal projections of the spline $S(x) = N^{-1/2} \sum_{n=0}^{N-1} \sigma_n \gamma_n(x) \in {}^p\mathcal{S}^{0,0}$

onto the subspaces ${}^p\mathcal{S}^{r,l}$. On the other hand, subsequent application of the relation (4.16) enables to derive the SHA spectra of splines from the subspaces ${}^p\mathcal{S}^{r,l}$.

4.3 Wavelet Packets: 1D

4.3.1 Definition of Spline Wavelet Packets

The complex-valued basis splines $\gamma_n^{r,l}(x)$ (4.9) are well localized in the frequency domain but their supports in the time domain occupy the whole interval $[0, N]$ (up to periodization). We introduce a family of orthonormal bases for the spline space ${}^p\mathcal{S}$, whose elements are real-valued and localized in time domain. Denote

$$\psi^{r,l}(x) \triangleq \sqrt{\frac{2^r}{N}} \sum_{n=0}^{N/2^r-1} \gamma_n^{r,l}(x) \in {}^p\mathcal{S}^{r,l}. \tag{4.17}$$

Proposition 4.3 *Translations $\{\psi^{r,l}(x - 2^r k)\}$, $k = 0, \dots, N/2^r - 1$, of the splines $\psi^{r,l}(x)$ form an orthonormal basis for ${}^p\mathcal{S}^{r,l}$. The translations $\{\psi^{r,l}(x - 2^r k)\}$, $l = 0, \dots, 2^r - 1$, $k = 0, \dots, N/2^r - 1$, form an orthonormal basis for the entire space ${}^p\mathcal{S}$.*

Proof The spline $\psi^{r,l}(x - 2^r k)$ is orthogonal to any spline $\psi^{r,\tilde{l}}(x - 2^r \tilde{k})$, for $\tilde{l} \neq l$. This is true because they belong to the mutually orthogonal subspaces. The inner product of two splines from the same subspace is

$$\begin{aligned} & \int_0^N \psi^{r,l}(x - 2^r k) \overline{\psi^{r,l}(x - 2^r \tilde{k})} dx \\ &= \frac{2^r}{N} \sum_{n,\tilde{n}=0}^{N/2^r-1} \omega^{-2^r(kn - \tilde{k}\tilde{n})} \int_0^N \gamma_n^{r,l}(x) \overline{\gamma_{\tilde{n}}^{r,l}(x)} dx \\ &= \frac{2^r}{N} \sum_{n=0}^{N/2^r-1} w^{-2^r n(k - \tilde{k})} = \delta_k^{\tilde{k}}, \quad k = 0, \dots, N/2^r - 1. \end{aligned} \quad \square$$

The splines $\psi^{r,0}(x)$ and $\psi^{r,1}(x)$ are the periodic Battle-Lemarié father and mother wavelets [5, 17], respectively. The splines $\psi^{r,l}(x)$ with arbitrary $l = 0, 1, \dots, 2^r - 1$, are periodic orthonormal wavelet packets.

4.3.2 The SHA Spectra of Spline Wavelet Packets

All the spaces ${}^p\mathcal{S}^{r,l} \subset {}^p\mathcal{S}$, thus, the wavelet packets belong to the initial spline space ${}^p\mathcal{S}^{0,0}$. To use them, we need to know the SHA spectra $\{v_n^{r,l}\}_{n=0}^{N-1}$ of these wavelet packets and their coordinates in the orthonormal basis $\{\gamma_n(x)\}$, $n = 0, \dots, N - 1$, of the space ${}^p\mathcal{S}$.

At the initial scale we have $\psi^{0,0}(x) = N^{-1/2} \sum_{n=0}^{N-1} \gamma_n(x) \implies v_n^{0,0} = 1$.

When $r > 0$, we derive the spectra using (4.16). Here are examples of the spectra of the first and second scales.

Wavelet packets from the first scale: For $m = 0, 1$, ${}^p\psi^{1,m}(x) = N^{-1/2} \sum_{n=0}^{N-1} v_n^{1,m} \gamma_n(x)$ where

$$\begin{aligned} v_n^{1,0} &= \sqrt{2} b_n^{0,0} = \sqrt{\frac{2^p u_n^0}{2^p u_n^1}} \cos^p\left(\frac{\pi n}{N}\right), \\ v_n^{1,1} &= \sqrt{2} b_n^{1,1} = \omega^n \sqrt{\frac{2^p u_{n+N/2}^0}{2^p u_n^1}} \sin^p\left(\frac{\pi n}{N}\right). \end{aligned}$$

Wavelet packets from the second scale: For $m = 0, 1, 2, 3$, ${}^p\psi^{1,l}(x) = N^{-1/2} \sum_{n=0}^{N-1} v_n^{2,m} \gamma_n(x)$ where

$$\begin{aligned} v_n^{2,0} &= \sqrt{2} b_n^{2,0} v_n^{1,0} = \sqrt{\frac{2^p u_n^1}{2^p u_n^2}} \cos^p\left(\frac{2\pi n}{N}\right) v_n^{1,0} \\ &= \sqrt{\frac{2^p u_n^0}{2^p u_n^2}} \cos^p\left(\frac{\pi n}{N}\right) \cos^p\left(\frac{2\pi n}{N}\right), \\ v_n^{2,1} &= \omega^{2n} \sqrt{\frac{2^p u_n^0}{2^p u_n^1} \frac{2^p u_{n+N/4}^1}{2^p u_n^2}} \cos^p\left(\frac{\pi n}{N}\right) \sin^p\left(\frac{2\pi n}{N}\right), \\ v_n^{2,2} &= \omega^n \sqrt{\frac{2^p u_{n+N/2}^0}{2^p u_n^2}} \sin^p\left(\frac{\pi n}{N}\right) \cos^p\left(\frac{2\pi n}{N}\right), \\ v_n^{2,3} &= \omega^{3n} \sqrt{\frac{2^p u_{n+N/2}^0}{2^p u_n^1} \frac{2^p u_{n+N/4}^1}{2^p u_n^2}} \\ &\quad \times \sin^p\left(\frac{\pi n}{N}\right) \sin^p\left(\frac{2\pi n}{N}\right). \end{aligned}$$

Similarly, the SHA spectra of the wavelet packets from the lower resolution scales are derived.

4.3.3 Structure of the SHA Spectra of Spline Wavelet Packets

Since the SHA spectra $\{\sigma_n\}_{n=0}^{N-1}$ of splines are the DFT of real sequences of the B-splines coefficients (up to real symmetric multipliers), then the sequence of absolute values $\{|\sigma_n|\}_{n=0}^{N-1}$ are symmetric about $N/2 - 1/2$. Therefore, it is sufficient to consider the spectra only for $n = 0, \dots, N/2 - 1$.

The coefficients of the wavelet packets of the initial scale are all 1. From (2.11) and (4.3), the coefficients are

$$\begin{aligned} v_n^{1,0} &= \sqrt{2} \frac{\sin^p(\pi n/N) (2\pi(n/N))^p}{\sin^p(2\pi n/N) (2\pi(n/N))^p} \cos^p\left(\frac{\pi n}{N}\right) \\ &\quad \times (1 + O(n^{-p})). \end{aligned}$$

Thus, it follows that $v_n^{1,0}/\sqrt{2}$ is close to one when n is small and monotonically decays to zero when n tends to $N/4$.

Fig. 1 *Right:* Wavelet packets of order 4 from the first resolution scale. *Left:* Their SHA spectra



Fig. 2 *Right:* Wavelet packets of order 10 from the first resolution scale. *Left:* Their SHA spectra

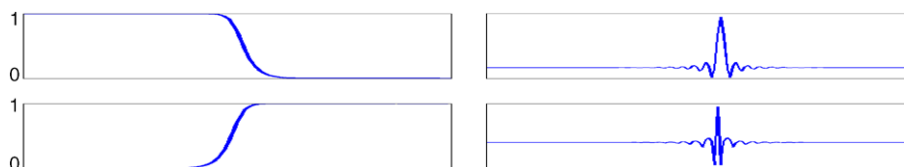


Fig. 3 *Right:* Wavelet packets of order 10 from the second resolution scale. *Left:* Their SHA spectra

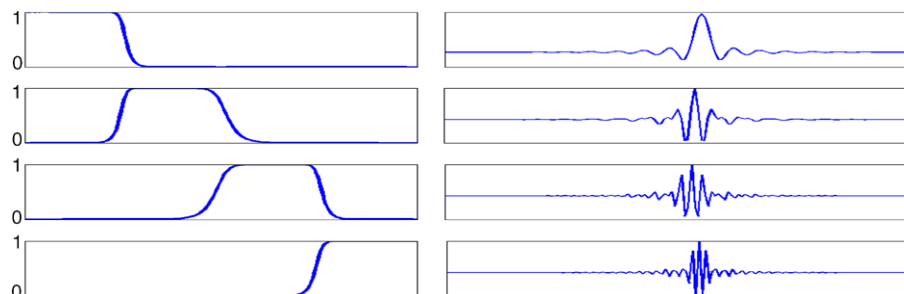
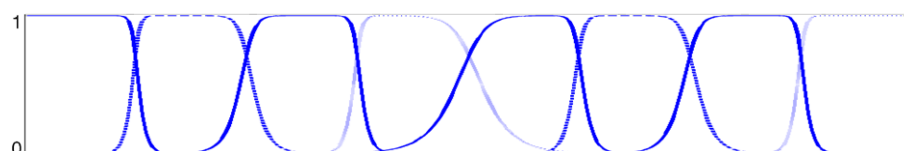


Fig. 4 The SHA spectra of wavelet packets of order 10 from the third resolution scale



The higher the order p of splines is, the closer the shape of the SHA spectrum $\{v_n^{1,0}/\sqrt{2}\}$ is to the rectangle $[0, N/4] \times [0, 1]$. We have $|v_n^{1,1}| = v_{n+N/2}^{1,0}$. Therefore, the magnitudes of the SHA spectrum $\{|v_n^{1,0}|/\sqrt{2}\}$ mirror the spectrum $\{v_n^{1,0}/\sqrt{2}\}$ about $N/4 - 1/2$. In other words, the SHA spectra $\{v_n^{1,0}/\sqrt{2}\}$ and $\{v_n^{1,1}/\sqrt{2}\}$ can be interpreted as the frequency responses of the half-band low-pass and high-pass digital filters, respectively. They split the full frequency band $[0, N/2 - 1]$ into two halves.

Similarly, the SHA spectra $\{v_n^{2,0}/2\}$ and $\{v_n^{2,1}/2\}$ of the wavelet packets from the second scale split the frequency band $[0, N/4 - 1]$ into two halves, whereas $\{v_n^{2,3}/2\}$ and $\{v_n^{2,2}/2\}$ halve the band $[N/4, N/2 - 1]$. The spectra of the wavelet packet coefficients from level r constitute a 2^r -band split of the interval $[0, N/2]$.

As a result from the above construction, we have a versatile library of symmetric waveforms of different shapes, smoothness and spans. They are not compactly supported but are well localized in time domain. Their SHA spectra are near rectangular and their supports produce a collection of different splits of the band $[-N/2, N/2]$. Since we have the expansions of these waveforms in terms of the orthonormal exponential spline bases $\{\gamma_n^p(x)\}_{n=0}^{N-1}$, then the operations of convolution, differentiation, translation and finding inner

products become straightforward. Therefore, it is only natural to use these waveforms to deal with the deconvolution problem. The practical computational cost of the operations does not depend on the order of the involved splines. Once the solution is found, it can be explicitly calculated at any point on the real axis.

We display in Figs. 1–4 the wavelet packets and their SHA spectra. Figures 1 and 2 compare the wavelet packets of the first resolution scale of orders 4 and 10, respectively. These are the Battle–Lemarié wavelets. One can observe that, while the wavelets of fourth order are better localized in time domain, the spectra of the tenth order wavelets are near rectangular. Figure 3 displays the wavelet packets of order 10 from the second resolution scale and their SHA spectra that split the frequency domain into four bands. In Fig. 4, we display the division of the frequency domain into eight bands by SHA spectra of the tenth order wavelet packets from the third resolution scale.

4.3.4 Wavelet Packets Bases

Assume that a spline $S^{r,l}(x) \in {}^pS^{r,l}$. Then, it can be expanded via the orthonormal wavelet packets basis. Equa-

tions (4.11) and (4.17) imply that

$$\begin{aligned}
 S^{r,l}(x) &= \sum_{k=0}^{N/2^r-1} s_k^{r,l} \psi^{r,l}(x - 2^r k) \\
 &= \sqrt{\frac{2^r}{N}} \sum_{k=0}^{N/2^r-1} s_k^{r,l} \sum_{n=0}^{N/2^r-1} \gamma_n^{r,l}(x - 2^r k) \\
 &= \sqrt{\frac{2^r}{N}} \sum_{n=0}^{N/2^r-1} \gamma_n^{r,l}(x) \sum_{k=0}^{N/2^r-1} \omega^{-2^r nk} s_k^{r,l} \\
 &= \sqrt{\frac{2^r}{N}} \sum_{n=0}^{N/2^r-1} \sigma_n^{r,l} \gamma_n^{r,l}(x). \tag{4.18}
 \end{aligned}$$

Thus, the coordinates of the spline $S^{r,l}(x) \in {}^p\mathcal{S}^{r,l}$ in two orthonormal bases of the space are linked via the DFT as

$$\begin{aligned}
 \sigma_n^{r,l} &= \sum_{k=0}^{N/2^r-1} \omega^{-2^r nk} s_k^{r,l}, \\
 s_k^{r,l} &= \frac{2^r}{N} \sum_{n=0}^{N/2^r-1} \omega^{2^r nk} \sigma_n^{r,l}. \tag{4.19}
 \end{aligned}$$

Assume that a spline $S(x) \in {}^p\mathcal{S}$ is represented by the wavelet packet expansion $S(x) = \sum_{k=0}^{N-1} s_k \psi(x - k)$. Then, its representation in exponential orthonormal basis $S(x) = N^{-1/2} \sum_{n=0}^{N-1} \sigma_n \gamma_n(x)$ is derived from the FFT calculations of the coefficients $\sigma_n = \sum_{k=0}^{N-1} \omega^{-nk} s_k$.

Iterated application of the relation (4.15) provides the coordinates $\sigma_n^{r,l}$ of the orthogonal projections $S^{r,l}(x)$ of the spline $S(x)$ onto the subspaces ${}^p\mathcal{S}^{r,l}$, $r = 1, \dots, R$, $l = 0, \dots, 2^r - 1$. Then, by utilizing (4.19), we find the coordinates $s_k^{r,l}$ in the wavelet packets bases $\{\psi^{r,l}(x - 2^r k)\}$ of the projections $S^{r,l}(x)$. These computations are fast, because they consist of forward and backward application of fast Fourier transform.

Once these coordinates are calculated, we are able to represent the spline $S(x)$ via variety of orthonormal bases, which are constituted by the wavelet packets $\{\psi^{r,l}(x - 2^r k)\}$ that belong to different combinations of the subspaces ${}^p\mathcal{S}^{r,l}$. In order to select an orthonormal basis, which provides, in a sense, an optimal representation of the spline $S(x)$, we implement the Best Basis algorithm [8, 9]. For this, we calculate the entropy cost function

$$E^{r,l} \triangleq - \sum_{k=0}^{N/2^r-1} \frac{|s_k^{r,l}|^2}{\|S\|^2} \log_e \frac{|s_k^{r,l}|^2}{\|S\|^2} \tag{4.20}$$

for all the subspaces ${}^p\mathcal{S}^{r,l}$. The Best Basis tree is derived by comparison between the entropies of the ‘‘parent’’ subspaces ${}^p\mathcal{S}^{r,l}$ and the entropies of the ‘‘offsprings’’ subspaces pair ${}^p\mathcal{S}^{r+1,2l} \cup {}^p\mathcal{S}^{r+1,2l+1}$.

5 Block Based Algorithm for Deconvolution: 1D Case

Assume we are given two vectors $\mathbf{z} = \{z_k\}$ and $\mathbf{h} = \{h(k)\}$, where $z_k = g(k) + e_k$, $h(x)$ and $g(x)$ are the kernel and the output of the convolution equation (2.1), respectively. The input function $f(x)$ has to be approximated. A global regularized solution to this problem was described in Sect. 3. The regularization parameter ρ for this solution was selected according to the relative contributions to the available signal \mathbf{z} from the input function $f(x)$ and from the noise. But these contributions are different for different frequency components of the signal \mathbf{z} . Therefore, to enhance the flexibility of the solution, we propose to solve the convolution equation separately for different frequency bands. The wavelet packet bases, which were described in Sect. 4, provide tools for fast implementation of this approach. To be specific, we approximate $f(x)$ by a spline from the space ${}^p\mathcal{S}$. This spline is a linear combination of the wavelet packets $\{\psi^{r,l}(x - 2^r k)\}$ that belong to different subspaces ${}^p\mathcal{S}^{r,l}$ of the spline space ${}^p\mathcal{S}$. For this we need to embed the basic operations such as convolution, inner products, etc into the subspaces ${}^p\mathcal{S}^{r,l}$.

5.1 Partial Solution of the Convolution Equation in the Subspace ${}^p\mathcal{S}^{r,l}$

5.1.1 Splines from the Subspaces ${}^p\mathcal{S}^{r,l}$

Assume that the spline $S(x) \in {}^p\mathcal{S}^{r,l}$. Then, it can be expanded via the orthonormal wavelet packets basis $\{\psi^{r,l}(x - 2^r k)\}$, where $\psi^{r,l}(x) = N^{-1/2} \sum_{n=0}^{N-1} v_n^{r,l} \gamma_n^p(x)$. By using (4.11), we get

$$\begin{aligned}
 S(x) &= \sum_{k=0}^{N/2^r-1} s_k \psi^{r,l}(x - 2^r k) \\
 &= \sqrt{\frac{1}{N}} \sum_{k=0}^{N/2^r-1} s_k \sum_{n=0}^{N-1} v_n^{r,l} \gamma_n^p(x - 2^r k) \\
 &= \sqrt{\frac{1}{N}} \sum_{n=0}^{N-1} v_n^{r,l} \sigma_n \gamma_n^p(x), \tag{5.1}
 \end{aligned}$$

where $\sigma_n = \hat{s}(n)$ is $N/2^r$ -periodic sequence. Grid points samples of the spline $S(x)$ are

$$S(k) = \frac{1}{N} \sum_{n=0}^{N-1} \sigma_n V_n^p v_n^{r,l} \omega^{nk} \implies \hat{S}(n) = \sigma_n V_n^p v_n^{r,l}. \tag{5.2}$$

It stems from the discussion in Sect. 4.3.3 that multiplication of the DFT $\{\hat{a}(n)\}$ of a vector $\mathbf{a} = \{a_k\}_{k=0}^{N-1} \in \mathbb{R}^N$ with the SHA spectrum $\{v_n^{r,l}\}$ of the wavelet packet $\psi^{r,l}(x)$ can be regarded as a band-pass filtering of this vector. Denote by

$\mathbb{R}^{r,l}$ the subset of \mathbb{R}^N , which consists of the “filtered” vectors $\mathbf{b} = \{b_k\}_{k=0}^{N-1}$, whose components can be represented as $b_k = N^{-1} \sum_{n=0}^{N-1} \omega^{kn} v_n^{r,l} \alpha_n$. Equation (5.2) implies that the vector $\{a_k\}_{k=0}^{N-1}$ belongs to $\mathbb{R}^{r,l}$. The same is true for the sampled convolution.

Assume that we have the spline

$$\chi(x) = \sqrt{\frac{1}{N}} \sum_{n=0}^{N-1} \mu_n \gamma_n^q(x) \in {}^q\mathcal{S}. \tag{5.3}$$

Proposition 5.1 *If the spline $S(x) \in {}^p\mathcal{S}^{r,l}$ then $\theta \triangleq \{\theta_k \triangleq \chi \star S(k)\}_{k=0}^{N-1}$ belongs to $\mathbb{R}^{r,l}$.*

Proof Let $S(x)$ be represented as in (5.1). Equation (2.26) implies that

$$\begin{aligned} \theta_k &= \frac{1}{N} \sum_{n=0}^{N-1} \sigma_n Q_n^{p,q} \mu_n v_n^{r,l} \omega^{nk} \\ \implies \hat{\theta}(n) &= \sigma_n Q_n^{p,q} \mu_n v_n^{r,l}. \end{aligned} \tag{5.4}$$

Thus, $\theta \in \mathbb{R}^{r,l}$. □

In other words, Proposition 5.1 claims that the DFT of the sampled convolution of a spline from ${}^p\mathcal{S}^{r,l}$ with a kernel spline lies within the spectral band defined by the SHA spectrum $\{v_n^{r,l}\}$. Thus, if we are looking for the solution’s component $S(x) \in {}^p\mathcal{S}^{r,l}$, then we have to use the component of the output data, which belongs to $\mathbb{R}^{r,l}$. For this, we filter the data array \mathbf{z} . The FFT $\hat{z}(n) = \sum_{k=0}^{N-1} \omega^{-nk} z_k$ is calculated. Denote

$$\hat{z}^{r,l}(n) = v_n^{r,l} \hat{z}(n), \quad z_k^{r,l} = \frac{1}{N} \sum_{n=0}^{N-1} \omega^{nk} \hat{z}^{r,l}(n). \tag{5.5}$$

5.1.2 Solution of the Minimization Problem in the Subspace ${}^p\mathcal{S}^{r,l}$

Assume that the spline $\chi(x)$, which interpolates the kernel data \mathbf{h} , is represented as in (5.3). Denote by $S_\rho(x) \in {}^p\mathcal{S}^{r,l}$ the spline, which minimizes the functional $J_\rho^{r,l}(S) \triangleq \rho I(S) + E^{r,l}(S)$, where $I(S) \triangleq \|S'\|^2$, $E^{r,l}(S) \triangleq \sum_{k=0}^{N-1} (\theta_k - z_k^{r,l})^2$, $\theta_k \triangleq \chi \star S(k)$ and ρ is a numerical parameter.

Assume that the spline $S(x) \in {}^p\mathcal{S}^{r,l}$ is represented as in (5.1). Due to (2.22) and (2.17),

$$\begin{aligned} I(S) &= \frac{1}{N} \sum_{n=0}^{N-1} |\sigma_n v_n^{r,l}|^2 W_n^{p,1}, \\ W_n^{p,1} &\triangleq \frac{u_n^{2(p-1)}}{u_n^{2p}} \left(2 \sin \frac{\pi n}{N} \right)^2. \end{aligned}$$

Equations (5.4) and (5.5) imply that $E^{r,l}(S) = N^{-1} \times \sum_{n=0}^{N-1} |v_n^{r,l} \sigma_n \mu_n Q_n^{p,q} - \hat{z}^{r,l}(n)|^2$ and the functional

$$\begin{aligned} N J_\rho^{r,l}(S) &= \sum_{n=0}^{N-1} (\rho |\sigma_n v_n^{r,l}|^2 W_n^{p,1} \\ &\quad + |\sigma_n v_n^{r,l} \mu_n Q_n^{p,q} - \hat{z}^{r,l}(n)|^2) \\ &= \sum_{n=0}^{N-1} |\sigma_n v_n^{r,l}|^2 (\rho W_n^{p,1} + |\mu_n Q_n^{p,q}|^2) \\ &\quad + 2^{-r+1} \mathcal{R}\mathcal{E}(\sigma_n \mu_n v_n^{r,l} Q_n^{p,q} \hat{z}^{r,l}(n)) \\ &\quad + |\hat{z}^{r,l}(n)|^2. \end{aligned} \tag{5.6}$$

The minimum of $J_\rho^{r,l}(S)$ is achieved when

$$\begin{aligned} \zeta_n^{r,l} &\triangleq \sigma_n v_n^{r,l} = \frac{\overline{\mu_n Q_n^{p,q} \hat{z}^{r,l}(n)}}{A_n(\rho)}, \\ A_n(\rho) &\triangleq W_n^{p,1} \rho + |\mu_n Q_n^{p,q}|^2, \\ Q_n^{p,q} &\triangleq \frac{u_n^{p+q}}{\sqrt{u_n^{2p} u_n^{2q}}}. \end{aligned} \tag{5.7}$$

Hence, the minimal spline

$$\begin{aligned} S_\rho(x) &= \sqrt{\frac{1}{N}} \sum_{n=0}^{N-1} \zeta_n^{r,l} \gamma_n^p(x) \in {}^p\mathcal{S}^{r,l}, \\ S_\rho(k) &= \frac{1}{N} \sum_{n=0}^{N-1} \omega^{kn} \frac{u_n^p \zeta_n^{r,l}}{\sqrt{u_n^{2p}}}. \end{aligned} \tag{5.8}$$

Thus, the values of the spline at the grid points are the IFFT of the sequence $\lambda_n^{r,l} \triangleq u_n^p \zeta_n^{r,l} (u_n^{2p})^{-1/2}$.

The convolution of the spline $S_\rho(x)$ with the kernel spline $\chi(x)$ defined in (5.3) is

$$\begin{aligned} \theta_\rho(x) &\triangleq \chi \star S_\rho(x) = \sqrt{\frac{1}{N}} \sum_{n=0}^{N-1} \mu_n U_n^{p,q} \zeta_n^{r,l} \gamma_n^{p+q}(x), \\ \theta_\rho(k) &= \frac{1}{N} \sum_{n=0}^{N-1} \omega^{kn} \mu_n Q_n^{p,q} \zeta_n^{r,l}. \end{aligned} \tag{5.9}$$

Thus, the values of the convolution at the grid points are found by IFFT of the sequence $\tau_n^{r,l} \triangleq \mu_n Q_n^{p,q} \zeta_n^{r,l}$.

5.1.3 Selection of the Regularization Parameter

Assume that we are able to evaluate the errors vector $\mathbf{e} = \{e_k\}_{k=0}^{N-1}$, $e_k = N^{-1} \sum_{n=0}^{N-1} \omega^{kn} \hat{e}(n)$, whose variance $\text{var}(\mathbf{e}) = \varepsilon^2 \approx N^{-1} \sum_{k=0}^{N-1} (e_k)^2$. Denote $\hat{e}^{r,l}(n) = v_n^{r,l} \hat{e}(n)$ and $e_k^{r,l} = N^{-1} \sum_{n=0}^{N-1} \omega^{nk} \hat{e}^{r,l}(n)$.

Denote $(\epsilon^{r,l})^2 \triangleq \sum_{k=0}^{N-1} (\epsilon_k^{r,l})^2 = N^{-1} \sum_{n=0}^{N-1} |\hat{e}^{r,l}(n)|^2$.
The function

$$\epsilon^{r,l}(\rho) \triangleq E^{r,l}(S_\rho) = \frac{1}{N} \sum_{n=0}^{N-1} \left(\frac{\rho |\hat{z}^{r,l}(n)| W_n^{p,1}}{A_n(\rho)} \right)^2$$

grows monotonically from zero to $N^{-1} \sum_{n=0}^{N-1} |\hat{z}^{r,l}(n)|^2 = \sum_{k=0}^{N-1} (z_k^{r,l})^2$ as ρ grows from zero to infinity. Therefore, we propose to derive $\rho^{m,l}$ from the equation $\epsilon^{r,l}(\rho) = (\epsilon^{r,l})^2$.

5.1.4 Modeling the Noise

We assume that the error vector \mathbf{e} is a zero mean Gaussian white noise. Typically, the convolution kernel $h(x)$ is efficiently bandlimited. Then, its significant Fourier coefficients $C_n(h)$ occupy a relatively narrow band around zero, $-K < n < K$, $K < N/2$. Hence, the FFT coefficients of the data vector $\mathbf{z}\{\hat{z}(n)\}_{n \in [K, N/2-1] \cup [-N/2, -K]} \approx \{\hat{e}(n)\}_{n \in [K, N/2-1] \cup [-N/2, -K]}$. By relying on the fact that the power spectrum $\{|\hat{e}(n)|^2\}$ of the white noise \mathbf{e} is close to a constant for all $n = -N/2, \dots, N/2 - 1$, we evaluate the variance

$$\sigma^2 \approx \frac{1}{(N - K)^2} \sum_{n \in [K, N/2-1] \cup [-N/2, -K]} |\hat{z}(n)|^2. \tag{5.10}$$

We model the noise vector as a zero mean Gaussian random process $\tilde{\mathbf{e}} = \{\tilde{e}_i\}_{i=0}^{N-1}$, whose variance is σ^2 . Let $\{\tilde{e}(n)\}_{n=0}^{N-1}$ be the FFT spectrum of the model vector $\tilde{\mathbf{e}}$. Then, we estimate the values $(\epsilon^{r,l})^2$, which are needed for the parameter ρ selection, as

$$(\epsilon^{r,l})^2 \approx \frac{1}{N} \sum_{n=0}^{N-1} |v_n^{r,l} \tilde{e}(n)|^2. \tag{5.11}$$

Remark 5.1 To make the estimation in (5.11) robust, it is advisable to calculate $(\epsilon^{r,l})^2$ several times using different realizations of the random process $\tilde{\mathbf{e}}$ and to average the results.

Another option for the noise evaluation is to use the scheme in [13].

5.2 Approximated Solution for the Convolution Equation in the Space ${}^p\mathcal{S}$

5.2.1 Selection of the Subspaces ${}^p\mathcal{S}^{r,l}$

It was mentioned in Sect. 5.1.1 that if we are looking for the solution’s component $S(x) \in {}^p\mathcal{S}^{r,l}$ then we have to use the output data from the subset $\mathbb{R}^{r,l}$. We select the relevant subspaces ${}^p\mathcal{S}^{r,l}$ in the following way:

1. Construct the spline

$$Z(x) = \sqrt{\frac{1}{N}} \sum_{n=0}^{N-1} v_n \gamma_n^p(x), \quad v_n = \frac{\hat{z}(n) \sqrt{u_n^{2p}}}{u_n^p}, \tag{5.12}$$

which interpolates the data \mathbf{z} .

2. Apply the spline coordinates transform of order p to the array $\{v_n\}$ down to the scale J as was defined in Sect. 4.2. This way we find the coordinates $\{v_n^{r,l}\}$ of the data spline projections onto all the subspaces ${}^p\mathcal{S}^{r,l}$, $r = 1, \dots, J$, $l = 0, \dots, 2^r - 1$.
3. Apply the Best Basis algorithm to the transform coefficients $\{v_n^{r,l}\}$. As a result, we obtain the list $RL = \{(\bar{r}, \bar{l})\}$ such that the shifts of the wavelet packets $\psi^{\bar{r}, \bar{l}}(x)$, $(\bar{r}, \bar{l}) \in RL$, form an optimal basis for the spline $Z(x)$. The list RL determines the subspaces ${}^p\mathcal{S}^{\bar{r}, \bar{l}}$, where we find the partial solutions of the convolution equation.
4. Since the kernel spline $\chi(x)$ is bandlimited, it may happen that the overlap of its SHA spectrum with some of the SHA spectra of the wavelet packets $\psi^{\check{r}, \check{l}}(x)$, $(\check{r}, \check{l}) \in RL$, is (almost) empty. It means that the data component $\mathbf{z}^{\check{r}, \check{l}} = \{z_k^{\check{r}, \check{l}}\}$ (see (5.5)) contains (almost) no contribution from the function $f(x)$ that we are looking for. Thus, the projection of the spline $Z(x)$ onto the subspaces ${}^p\mathcal{S}^{\check{r}, \check{l}}$ are pure noise. To detect such “empty” subspaces, we calculate the norms of the splines $\Psi^{\bar{r}, \bar{l}}(x) \triangleq \chi \star \psi^{\bar{r}, \bar{l}}(x)$, $(\bar{r}, \bar{l}) \in RL$ and define some threshold T . We reduce the list of subspaces RL to the shorter list \overline{RL} by discarding the pairs (\check{r}, \check{l}) such that the norms $\|\Psi^{\check{r}, \check{l}}\| < T$.

5.2.2 Scheme for the Approximated Solution of the Convolution Equation (2.1)

- Evaluate the error vector that means to estimate the partial variances $(\epsilon^{r,l})^2$ of noise (5.11).
- Construct the kernel spline $\chi(x)$ (5.3).
- Construct the data spline $Z(x)$ (5.12).
- Implement the transform of order p of the spline $Z(x)$ coordinates (Sect. 4.2).
- Apply the Best Basis algorithm to the transform coefficients.
- Define the reduced list $\overline{RL} = \{(\bar{r}, \bar{l})\}$ of the appropriate subspaces.
- Determine the optimal values $\rho_{\bar{r}, \bar{l}}$ of the regularization parameter for each pair $(\bar{r}, \bar{l}) \in \overline{RL}$ (Sect. 5.1.4).
- Find the partial solutions $S_{\rho_{\bar{r}, \bar{l}}}(x) \in {}^p\mathcal{S}^{\bar{r}, \bar{l}}$ for each pair $(\bar{r}, \bar{l}) \in \overline{RL}$ (5.8).

The approximated solution to (2.1) is $S(x) = \sum_{(\bar{r}, \bar{l}) \in \overline{RL}} S_{\rho_{\bar{r}, \bar{l}}}(x) \in {}^p\mathcal{S}$.

6 Block Based Algorithm for Deconvolution: Outline of the 2D Case

As in Sect. 3.2, we assume that $\mathbf{z} = \{z_{k,n}\}$ and $\mathbf{h} = \{h(k, n)\}_{k,n=0}^{N-1}$ are the available data arrays. We assume that the x and y components of the 2D splines have the same order. Thus, $S^p(x, y)$ will stand for $S^{p,p}(x, y) \in {}^{p,p}\mathcal{S}$. We approximate the solution $f(x, y)$ of (2.2) by a spline from the space ${}^{p,p}\mathcal{S}$, which is a linear combination of the 2D wavelet packets that belong to different subspaces of the spline space ${}^{p,p}\mathcal{S}$.

6.1 2D Wavelet Packets

Denote $\gamma_{\kappa,t}^{r,l,\tilde{l}}(x, y) \triangleq \gamma_{\kappa}^{r,l}(x) \gamma_t^{r,\tilde{l}}(y)$. Obviously, the splines ${}^p\gamma_{\kappa,t}^{r,l,\tilde{l}}(x, y)$ with the same scale index r are mutually orthogonal and their norms are equal to 1. The 2D spline space ${}^{p,p}\mathcal{S}^{r,l,\tilde{l}} \subset {}^{p,p}\mathcal{S}$ is defined as the linear span of the splines $\gamma_{\kappa,t}^{r,l,\tilde{l}}(x, y), l, \tilde{l} = 0, \dots, N/2^r - 1$:

$$S(x, y) = \frac{2^{2r}}{N} \sum_{\kappa,t} \sigma_{\kappa,t}^{r,l,\tilde{l}} \gamma_{\kappa,t}^{r,l,\tilde{l}}(x, y) \in {}^{p,p}\mathcal{S}^{r,l,\tilde{l}}. \tag{6.1}$$

The splits (4.12) of the 1D spline spaces generate the splits of the space ${}^{p,p}\mathcal{S}$ into mutually orthogonal subspaces:

$$\begin{aligned} {}^{p,p}\mathcal{S}^{r-1,l,\tilde{l}} &= {}^{p,p}\mathcal{S}^{r,2l,\tilde{2}l} \oplus {}^{p,p}\mathcal{S}^{r,2l+1,\tilde{2}l} \oplus {}^{p,p}\mathcal{S}^{r,2l,\tilde{2}l+1} \\ &\quad \oplus {}^{p,p}\mathcal{S}^{r,2l+1,\tilde{2}l+1} \\ \implies {}^{p,p}\mathcal{S} &= \bigoplus_{r,l,\tilde{l}} {}^{p,p}\mathcal{S}^{r,l,\tilde{l}}, \end{aligned}$$

$r = 1, \dots, J, l, \tilde{l} = 0, \dots, N/2^r - 1$. Together with the orthonormal bases $\{\gamma_{\kappa,t}^{r,l,\tilde{l}}(x, y)\}, \kappa, t = 0, \dots, N/2^r$, of the subspaces ${}^{p,p}\mathcal{S}^{r,l,\tilde{l}} \subset {}^{p,p}\mathcal{S}$, there exist orthonormal bases

that consist of 2D wavelet packets shifts

$$S(x, y) = \sum_{k,n=0}^{N/2^r-1} s_{k,n}^{r,l,\tilde{l}} \psi^{r,l,\tilde{l}}(x - 2^r k, y - 2^r n) \in {}^{p,p}\mathcal{S}^{r,l,\tilde{l}}, \tag{6.2}$$

where

$$\begin{aligned} \psi^{r,l,\tilde{l}}(x, y) &\triangleq \psi^{r,l}(x) \psi^{r,\tilde{l}}(y) = \frac{1}{N} \sum_{\kappa,t} {}^p\gamma_{\kappa,t}^{r,l,\tilde{l}}(x, y), \\ s_{k,n}^{r,l,\tilde{l}} &= \frac{2^{2r}}{N^2} \sum_{\kappa,t} \omega^{2^r(n+k\kappa)} \sigma_{\kappa,t}^{r,l,\tilde{l}}. \end{aligned} \tag{6.3}$$

Each wavelet packet can be expanded via the orthonormal basis $\{\gamma_{\kappa,t}(x, y) = \gamma_{\kappa}(x) \gamma_t(y)\}$ of the initial space ${}^{p,p}\mathcal{S}$:

$$\psi^{r,l,\tilde{l}}(x, y) = \frac{1}{N} \sum_{\kappa,t=0}^{N-1} v_{\kappa,t}^{r,l,\tilde{l}} \gamma_{\kappa,t}^p(x, y)$$

and its SHA spectrum $\{v_{\kappa,t}^{r,l,\tilde{l}} = v_{\kappa}^{r,l} v_t^{r,\tilde{l}}\}$ is the tensor product of the SHA spectra of the 1D wavelet packets $\psi^{r,l}(x)$ and $\psi^{r,\tilde{l}}(y)$. We display in Fig. 5 the SHA spectra of two wavelet packets of order 10 from the second scale. One can observe that the spectra have near-parallelepiped shape. The spline $S(x) \in {}^{p,p}\mathcal{S}^{r,l,\tilde{l}}$, which is expanded as in (6.1) and (6.2), has the following representation in the initial space ${}^{p,p}\mathcal{S}$

$$S(x, y) = \frac{1}{N} \sum_{\kappa,t=0}^{N-1} \sigma_{\kappa,t}^{r,l,\tilde{l}} v_{\kappa,t}^{r,l,\tilde{l}} \gamma_{\kappa,t}(x, y). \tag{6.4}$$

Assume the spline $\tilde{S}(x, y) = N^{-1} \sum_{\kappa,t=0}^{N-1} \tilde{\sigma}_{\kappa,t} \gamma_{\kappa,t}^p(x, y) \in {}^{p,p}\mathcal{S}$ is expanded by the orthonormal basis of the space ${}^{p,p}\mathcal{S}$. Then, the wavelet packet coefficients $\{\tilde{\sigma}_{\kappa,t}^{r,l,\tilde{l}}\}$ of the projection of the spline onto all the spaces ${}^{p,p}\mathcal{S}^{r,l,\tilde{l}}, r = 1, \dots, J, l, \tilde{l} = 0, \dots, 2^r - 1$, are calculated via the application of the 2D transform of the coordinates $\{\sigma_{\kappa,t}\}$. The 2D transform is

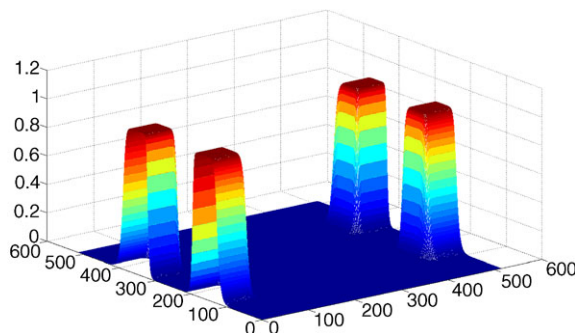
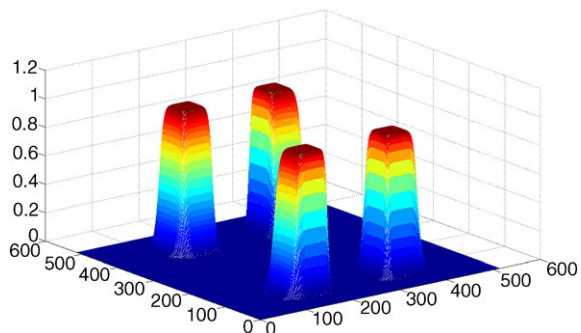


Fig. 5 The SHA spectra of wavelet packets of order 10 from the second resolution scale *Left*: $\psi^{2,2,3}(x, y)$. *Right*: $\psi^{2,3,1}(x, y)$

implemented by an iterated application of the 1D transform subsequently to the rows and columns of the array $\{\sigma_{\kappa,t}\}$.

The 2D wavelet packets $\{\psi^{r,l,\tilde{l}}(x - 2^r k, y - 2^r n)\}$, which belong to different subspaces ${}^{p,p}\mathcal{S}^{r,l,\tilde{l}}$ of the spline space ${}^{p,p}\mathcal{S}$, provide a variety of orthonormal bases of this space. To apply the Best Basis methodology in this case, we compare the entropies of the wavelet packet coefficients $\{s_{k,n}^{r-1,l,\tilde{l}}\}$ of the projection of a spline onto the “parent” spaces ${}^{p,p}\mathcal{S}^{r-1,l,\tilde{l}}$ with these for the projection onto the “off-spring” spaces ${}^{p,p}\mathcal{S}^{r,2l,\tilde{2l}}$, ${}^{p,p}\mathcal{S}^{r,2l+1,\tilde{2l}}$, ${}^{p,p}\mathcal{S}^{r,2l,\tilde{2l+1}}$ and ${}^{p,p}\mathcal{S}^{r,2l+1,\tilde{2l+1}}$.

6.2 Partial Solution of the Convolution Equation in ${}^{p,p}\mathcal{S}^{r,l,\tilde{l}}$

Define the functional $I(S) \triangleq \|S'_x\|^2 + \|S'_y\|^2$ in the spline space ${}^{p,p}\mathcal{S}$. If the spline $S(x)$ belongs to the subspace ${}^{p,p}\mathcal{S}^{r,l,\tilde{l}}$ then

$$I(S) = \frac{1}{N^2} \sum_{\kappa,t=0}^{N-1} |\sigma_{\kappa,t}^{r,l,\tilde{l}} v_{\kappa,t}^{r,l,\tilde{l}}|^2 (W_{\kappa}^{p,1} + W_t^{p,1}), \tag{6.5}$$

$$W_n^{p,1} \triangleq \frac{u_n^{2(p-1)}}{u_n^{2p}} \left(2 \sin \frac{\pi n}{N}\right)^2.$$

Let the spline $\chi(x, y) = N^{-1} \sum_{v,t=0}^{N-1} \mu_{v,t} \gamma_{v,t}^q(x) \in {}^{q,q}\mathcal{S}$ interpolates the kernel $h(x, y)$. Then,

$$\chi \star S(x, y) = \frac{1}{N} \sum_{\kappa,t=0}^{N-1} \mu_{v,t} \sigma_{\kappa,t}^{r,l,\tilde{l}} v_{\kappa,t}^{r,l,\tilde{l}} U_{\kappa}^{p,q} U_t^{p,q} \gamma_{v,t}^{p+q}(x) \in {}^{p+q,p+q}\mathcal{S},$$

$$U_n^{p,q} \triangleq \sqrt{\frac{u_n^{2(p+q)}}{u_n^{2p} u_n^{2q}}}.$$

As in 1D case, the data array is filtered. Denote $\hat{z}^{r,l,\tilde{l}}(\kappa, t) = v_{\kappa,t}^{r,l,\tilde{l}} \hat{z}(\kappa, t)$, where $\hat{z}(\kappa, t) = \sum_{k,n=0}^{N-1} \omega^{-(k\kappa+nt)} \times z_{k,n}$, and $z_k^{r,l,\tilde{l}} = N^{-2} \sum_n^j \omega^{(k\kappa+nt)} \hat{z}^{r,l,\tilde{l}}(\kappa, t)$.

Define the functional in the subspace ${}^{p,p}\mathcal{S}^{r,l,\tilde{l}}$

$$E^{r,l,\tilde{l}}(S) \triangleq \sum_{k,n=0}^{N-1} (\chi \star S(k, n) - z_{k,n}^{r,l,\tilde{l}})^2 = \frac{1}{N^2} \sum_{\kappa,t=0}^{N-1} |v_{\kappa,t}^{r,l,\tilde{l}} \sigma_{\kappa,t}^{r,l,\tilde{l}} Q_{\kappa}^{p,q} Q_t^{p,q} - \hat{z}^{r,l,\tilde{l}}(\kappa, t)|^2,$$

$$Q_n^{p,q} \triangleq \frac{u_n^{(p+q)}}{\sqrt{u_n^{2p} u_n^{2q}}}.$$

The spline

$$S_{\rho}(x, y) = \frac{1}{N} \sum_{\kappa,t=0}^{N-1} \zeta_{\kappa,t}^{r,l,\tilde{l}} \gamma_{\kappa,t}^p(x, y), \quad \text{where}$$

$$\zeta_{\kappa,t}^{r,l,\tilde{l}} = \frac{\bar{\mu}_{v,t} Q_{\kappa}^{p,q} Q_t^{p,q} \hat{z}^{r,l,\tilde{l}}(\kappa, t)}{A_{v,t}(\rho)},$$

$$A_{v,t}(\rho) \triangleq \rho(W_{\kappa}^{p,1} + W_t^{p,1}) + |\mu_{v,t} Q_{\kappa}^{p,q} Q_t^{p,q}|^2,$$

minimizes the functional $J_{\rho}^{r,l,\tilde{l}}(S) \triangleq \rho I(S) + E^{r,l,\tilde{l}}(S)$. The values of the spline $S_{\rho}(x, y)$ at the grid points $S_{\rho}(k, n) = N^{-2} \sum_{\kappa,t=0}^{N-1} \omega^{(k\kappa+nt)} \zeta_{\kappa,t}^{r,l,\tilde{l}} u_{\kappa}^p u_t^p / \sqrt{u_{\kappa}^{2p} u_t^{2p}}$ are calculated via the application of the 2D IFFT of the sequence $\lambda_{\kappa,t}^{r,l,\tilde{l}} \triangleq \zeta_{\kappa,t}^{r,l,\tilde{l}} u_{\kappa}^p u_t^p / \sqrt{u_{\kappa}^{2p} u_t^{2p}}$.

Selection of the Regularization Parameter: Like in Sect. 5.1.4, we evaluate the zero-mean errors array $\mathbf{e} = \{e_{k,n}\}_{k,n=0}^{N-1}$, $e_{k,n} = N^{-2} \sum_{\kappa,t=0}^{N-1} \omega^{(k\kappa+nt)} \hat{e}(\kappa, t)$, whose variance $\text{var}(\mathbf{e}) = \varepsilon^2 \approx N^{-2} \sum_{k,n=0}^{N-1} (e_{k,n})^2$. Denote $\hat{e}^{r,l,\tilde{l}}(\kappa, t) = v_{\kappa,t}^{r,l,\tilde{l}} \hat{e}(\kappa, t)$. Then,

$$e_k^{r,l} = \frac{1}{N^2} \sum_{\kappa,t=0}^{N-1} \omega^{(k\kappa+nt)} \hat{e}(\kappa, t),$$

$$(\varepsilon^{r,l,\tilde{l}})^2 \triangleq \sum_{k,n=0}^{N-1} (e_{k,n}^{r,l,\tilde{l}})^2 = \frac{1}{N^2} \sum_{\kappa,t=0}^{N-1} |\hat{e}^{r,l,\tilde{l}}(\kappa, t)|^2.$$

We derive an optimal value $\rho^{r,l,\tilde{l}}$ from the equation $\varepsilon^{r,l,\tilde{l}}(\rho) = (\varepsilon^{r,l,\tilde{l}})^2$, where the function

$$\begin{aligned} \varepsilon^{r,l,\tilde{l}}(\rho) &\triangleq E^{r,l,\tilde{l}}(\tilde{S}_{\rho}) \\ &= \frac{1}{N^2} \sum_{\kappa,t=0}^{N-1} \left(\frac{|\rho| \hat{z}^{r,l,\tilde{l}}(\kappa, t) | (W_{\kappa}^{p,1} + W_t^{p,1})}{A_{\kappa,t}(\rho)} \right)^2 \end{aligned}$$

grows monotonically.

6.3 Scheme for the Approximated Solution of the Convolution Equation in the Space ${}^{p,p}\mathcal{S}$

Best Basis Algorithm (BBA):

1. Evaluate the error array \mathbf{e} .
2. Construct the spline $\chi(x, y) \in {}^{q,q}\mathcal{S}$ that interpolates the kernel $h(x, y)$.
3. Construct the spline $Z(x, y) \in {}^{p,p}\mathcal{S}$ that interpolates the data array \mathbf{z} .
4. Implement the 2D transform of order p of the spline $Z(x, y)$ coordinates.

5. Apply the Best Basis algorithm to the transform coefficients.
6. Estimate the overlap of the SHA spectra of the wavelet packets $\psi^{\bar{r}, \bar{l}, \bar{l}}(x, y)$, which constitute the Best Basis, with the spectrum of the kernel spline $\chi(x, y)$. Discard the subspaces related to the wavelet packets whose spectra overlap with the χ spectrum is negligible.
7. Define the reduced list $\overline{RL} = \{(\bar{r}, \bar{l}, \bar{l})\}$ of the appropriate subspaces.
8. Determine the optimal values $\rho_{\bar{r}, \bar{l}, \bar{l}}$ of the parameter for each triple $(\bar{r}, \bar{l}, \bar{l}) \in \overline{RL}$.
9. Find the partial solutions $\tilde{S}_{\rho_{\bar{r}, \bar{l}, \bar{l}}}(x, y) \in {}^p\mathcal{S}^{\bar{r}, \bar{l}}$ for each pair $(\bar{r}, \bar{l}) \in \overline{RL}$.
10. The approximated solution to (2.1) is

$$S(x, y) = \sum_{\bar{r}, \bar{l}, \bar{l}} S_{\rho_{\bar{r}, \bar{l}, \bar{l}}}(x, y) \in {}^{p \cdot p}\mathcal{S}.$$

A Variation of BBA—Block Pursuit Algorithm (BPA):

1. Evaluate the error array \mathbf{e} .
2. Construct the spline $\chi(x, y) \in {}^{q \cdot q}\mathcal{S}$ that interpolates the kernel $h(x, y)$.
3. Let $\mathbf{z}^0 = \mathbf{z}$ and $S^0(x, y) \equiv 0$.
4. Construct the spline $Z^0(x, y) \in {}^{p \cdot p}\mathcal{S}$ that interpolates the array \mathbf{z}^0 .
5. Implement the 2D transform of order p of the spline $Z^0(x, y)$ coordinates.
6. Select a single subspace ${}^{p \cdot p}\mathcal{S}^{\bar{r}, \bar{l}, \bar{l}}$ such that the L_2 norm of the projection of $Z(x, y)$ onto this subspace is maximal.
7. Estimate the overlap of the SHA spectra of the wavelet packet $\psi^{\bar{r}, \bar{l}, \bar{l}}(x, y)$ with the spectrum of the kernel spline $\chi(x, y)$.
8. Determine the optimal values $\rho_{\bar{r}, \bar{l}, \bar{l}}$ of the parameter for the selected subspace ${}^{p \cdot p}\mathcal{S}^{\bar{r}, \bar{l}, \bar{l}}$.
9. Find the partial solutions $\tilde{S}_{\rho_{\bar{r}, \bar{l}, \bar{l}}}(x, y) \in {}^p\mathcal{S}^{\bar{r}, \bar{l}}$.
10. Let $S^1(x, y) \triangleq S^0(x, y) + \tilde{S}_{\rho_{\bar{r}, \bar{l}, \bar{l}}}(x, y)$.
11. Calculate $\theta_{k,n} \triangleq \eta \star \tilde{S}_{\rho_{\bar{r}, \bar{l}, \bar{l}}}(k, n)$.
12. Put $\mathbf{z}^1 \triangleq \{z_{k,n}^0 - \theta_{k,n}\}$.
13. The algorithm stops when the overlap of the SHA spectra of the wavelet packet $\psi^{\bar{r}, \bar{l}, \bar{l}}(x, y)$, which is selected at some iteration, with the spectrum of the kernel spline $\chi(x, y)$ becomes negligible.
14. Iterate the procedures starting from Item 4 using \mathbf{z}^1 instead of \mathbf{z}^0 .

Output: The approximated solution to (2.1) is

$$S(x, y) = \sum_{\bar{r}, \bar{l}, \bar{l}} S_{\rho_{\bar{r}, \bar{l}, \bar{l}}}(x, y) \in {}^{p \cdot p}\mathcal{S}.$$

Remark 6.1 The described algorithms can be utilized for signals and images denoising when the convolution is not present. In this case, the general scheme remains unchanged with the exception that the kernel array \mathbf{h} is reduced to $\delta(k)$ for 1D signals and to $\delta(k, n)$ for images. In this case, the approximated solution produced by the global Tikhonov algorithm, which was described in Sect. 3, is the so-called smoothing spline [25].

Remark 6.2 The Block Pursuit algorithm, which is somewhat related to the Matching Pursuit [18], is much more computationally expensive compared to BBA but, typically, it produces more accurate results for the pure deconvolution (without noise).

7 Numerical Experiments

We conducted a number of experiments to demonstrate the performance of the proposed solution for the convolution equations in one and two dimensions. Three groups of experiments were carried out:

Denoising: Restoration of objects corrupted by Gaussian noise.

Pure deconvolution: Restoration of objects blurred by convolution with a band-limited kernel. In this case, the contribution of the input signal into the stop-band of the kernel is not available. In addition, although noise is not introduced, some measurements errors present. Therefore, the problem remains ill-posed. The advantage of the block based methods over the global ones consists in the accurate tuning the subspaces where the solution is looked for to the pass-band of the kernel. The Block Pursuit Algorithm does this more precisely compared to the Best Basis Algorithm due to wider choice of the available subspaces.

Noised deconvolution: Restoration of objects blurred by convolution and corrupted by Gaussian noise.

In order to reduce the size of the paper, we present only image restorations results. We compared between the performance of the Best Basis Algorithm (BBA) and the Standard Regularized Deconvolution Algorithm (SRA). SRA was implemented by using the Matlab function `deconvreg`. For the examples on pure deconvolution we present the results from the application of the Block Pursuit Algorithm (BPA), which produces the most accurate restoration of images at the cost of excessive computational load. In the experiments where noise was present, BPA did not outperform BBA. We compared the visual results and the Peak Signal to Noise Ratio (PSNR) in decibels

$$\text{PSNR} \triangleq 10 \log_{10} \left(\frac{NM^2}{\sum_{k=1}^N (x_k - \tilde{x}_k)^2} \right) \text{dB}$$

Fig. 6 Barbara. *Top left:* Original; *Top right:* Noised image, $STD = 25$; *Center left:* Restored by SRA, $PSNR = 24.63$. *Bottom left:* Fragment of the image restored by SRA. *Center right:* Restored by BBA, $PSNR = 26.27$. Spline wavelet packets of the fourth order from 3 scales were used. *Bottom right:* Fragment of the image restored by BBA



where $\{x_k\}_{k=1}^N$ are the original samples of the signal (image), $M = \max_k |x_k|$ while $\{\tilde{x}_k\}_{k=1}^N$ are the restored samples of the signal (image).

All the images are of size 512×512 pixels.

7.1 Denoising Experiments

As was mentioned in Remark 6.1, the BBA restores noised images, which were not subjected to convolution.

Barbara denoising: We restored the Barbara image, which was corrupted by Gaussian zero-mean noise with different standard deviations (STD). The PSNR results are given in Table 1.

We see that BBA produces higher PSNR values in comparison to SRA. Visually, it provides better resolution of the image details. Figure 6 displays the restored image from an input image affected by noise with $STD = 25$.

Boats denoising: The Boats image, which was corrupted by Gaussian zero-mean noise with different standard devia-

Fig. 7 Boats. *Top left:* Original. *Top right:* Noised image, $STD = 25$. *Bottom left:* Fragment of the image restored by SRA, $PSNR = 27.26$. *Bottom right:* Fragment of the image restored by BBA, $PSNR = 27.27$. Spline wavelet packets of the fourth order from 3 scales were used

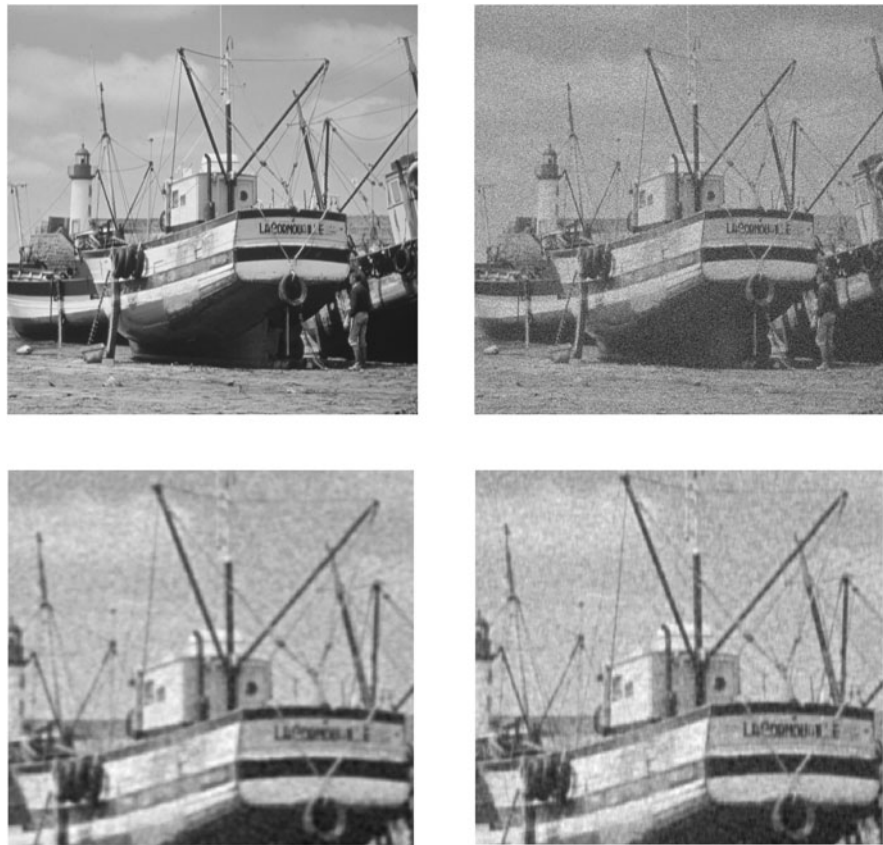


Table 1 PSNR values for the Barbara image that was restored from noised inputs

STD/PSNR	10/28.13	15/24.6	25/20.17	50/14.15
SRA	28.7	26.61	24.63	23.02
BBA	30.86	28.65	26.27	23.58
Spline order/scale	10/3	8/3	4/3	4/3

Table 2 PSNR values of the restored Boats image from noised inputs

STD/PSNR	10/28.13	15/24.6	25/20.17	50/14.15
SRA	31.2	29.35	27.26	24.78
BBA	31.75	30.01	27.80	24.90
Spline order/scale	10/3	4/2	4/3	4/3

tions (STD), was restored. The PSNR results are given in Table 2.

We see that BBA produces higher PSNR values in comparison to SRA for all the noise patterns except for noise with $STD = 50$. Visually, it provides better resolution of the image details. The restoration of the image from the input, which was affected by noise with $STD = 25$, is displayed in Fig. 7.

Table 3 The ePSNR values of the restored Lena image from blurred inputs

STD/PSNR	3/25.65	5/23.42	10/20.61	15/19.11
SRA	33.77	29.55	25.61	23.79
BBA	36.67	32.01	27.33	25.26
Spline order/scale	4/1	10/2	10/2	10/2
BPA	35.41	32.7	27.83	25.54
Spline order/scale	4/4	4/2	6/4	4/4

7.2 Pure Deconvolution Experiments

The presented algorithms proved to be highly efficient for image restoration, which were convolved with Gaussian kernels. Noise was not added. Following are a few examples.

Lena pure deconvolution: We restored the Lena image, which was blurred by convolving with Gaussian kernels with different standard deviations (STD). The PSNR results are given in Table 3.

As in the denoising experiments, BBA produces higher PSNR values in comparison to SRA. Visually, it provides better resolution for the image details. In most cases, BPA restores the image even better than BBA but its computational cost is incomparably higher than that of BBA. Restoration of the image from the input, which

Fig. 8 Lena. *Top left*: Original. *Top right*: Lena blurred by kernel with $STD = 10$, $PSNR = 20.61$. *Center left*: Fragment of the image restored by SRA, $PSNR = 25.61$. *Center right*: Fragment of the image restored by BBA, $PSNR = 27.33$. Spline wavelet packets of the tenth order from two scales were used. *Bottom left*: Fragment of the original image. *Bottom right*: Fragment of the image restored by BPA, $PSNR = 27.83$. Spline wavelet packets of the fourth order from two scales were used



was blurred by a kernel with $STD = 10$, is displayed in Fig. 8.

We observe that, in spite of having strongly blurred input, BBA and BPA provided a satisfactorily restored image. This is not true for the performance of SRA. BBA and, especially, BPA produce much less oscillating artefacts than SRA.

Barbara pure deconvolution: Barbara image, which was blurred by convolution with Gaussian kernels with different standard deviations (STD), was restored. The $PSNR$ results are given in Table 4. BBA produces higher $PSNR$

values in comparison with SRA. Visually, it provides better resolution of the image details. Figure 9 displays the restoration of the image from the input that was blurred by a kernel with $STD = 3$. We observe that texture resolved by BBA and BPA is better than what was resolved by SRA. In addition, contrary to SRA, they do not produce artefacts (on the face and hands, for example). The restoration by BPA is almost perfect.

Camerman pure deconvolution: We restored the Camerman image, which was blurred by convolution with

Fig. 9 Barbara. *Top left:* Original. *Top right:* Barbara blurred by kernel with $STD = 3$, $PSNR = 22.84$. *Center left:* Fragment of Barbara restored by SRA, $PSNR = 24.86$. *Center right:* Fragment of Barbara restored by BBA, $PSNR = 27.17$. Spline wavelet packets of the fourth order from one scale were used. *Bottom left:* Fragment of the original Barbara. *Bottom right:* Fragment of Barbara restored by BPA, $PSNR = 28.3$. Spline wavelet packets of the fourth order from three scales were used



Table 4 PSNR values of the restored Barbara image from blurred inputs

STD/PSNR	3/22.84	5/21.71	10/19.8	15/18.6
SRA	24.86	24.05	22.89	21.92
BBA	27.17	24.55	23.47	22.71
Spline order/scale	4/1	10/1	10/2	10/2
BPA	28.3	24.7	23.60	22.87
Spline order/scale	4/3	4/3	4/3	4/3

Table 5 PSNR values for the restored Cameraman image from blurred inputs

STD/PSNR	3/22.61	5/21.08	10/19.0	15/17.95
SRA	28.62	25.62	22.45	21.08
BBA	30.57	27.48	23.75	22.18
Spline order/scale	4/1	4/1	10/1	4/2
BPA	31.04	27.98	24.14	22.41
Spline order/scale	4/3	4/3	4/3	4/4

Gaussian kernels with different standard deviations (STD). The PSNR results are given in Table 5.

BBA and especially BPA produce higher PSNR values in comparison to SRA. Visually, it provides better resolution of the image details. Figure 10 displays the restored image from an input that was blurred by kernel with $STD = 5$. We see that the image restored by SRA contains some ringing artefacts, which, to a

lesser extent, takes place in the BBA restoration. However, the image restored by BPA is free from these artefacts. It is hardly distinguishable from the original image.

7.3 Noised Deconvolution Experiments

In the third series of experiments, we applied the Best Basis algorithm to restore images, which were convolved with

Fig. 10 Cameraman. *Top left:* Original. *Top right:* Cameraman was blurred by kernel with $STD = 5$, $PSNR = 21.08$. *Center left:* Fragment of the restored Cameraman by SRA, $PSNR = 25.62$. *Center right:* Restored Cameraman by BBA, $PSNR = 27.48$. Spline wavelet packets of fourth order from 1 scale were used. *Bottom left:* Original. *Bottom:* Restored Cameraman by BPA, $PSNR = 27.98$. Spline wavelet packets of fourth order from 3 scales were used



Gaussian kernels. In addition, the images were corrupted by zero-mean Gaussian noise. Following are a few examples.

Goldhill noised deconvolution: The Goldhill image, which was blurred by convolution with different Gaussian kernels and was corrupted by noise with constant $STD = 2$, was restored. Table 6 presents the PSNR results where Gaussian noise was constant with $STD = 2$ while blurring varied.

In all the experiments, BBA produces higher PSNR values in comparison to SRA. Visually, it provides better resolution of the image details. Figure 11 displays the restored Goldhill from the input blurred by a kernel with $STD = 3$ and corrupted by a Gaussian noise with $STD = 2$.

Table 6 PSNR values for the restored Goldhill image from noise ($STD = 2$) and blurred with variable Gaussian kernels

STD(kernel)/PSNR	1/26.68	2/26.5	3/25.08	4/24.09	5/23.32
SRA	31.63	28.61	27	26.04	25.38
BBA	32.34	28.96	27.36	26.20	25.46
Spline order/scale	8/1	12/2	4/2	4/2	4/2

We observe that, set aside higher PSNR, the BBA-restored image is cleaner and sharper in comparison to the image restored by SRA.

Fig. 11 Goldhill. *Top left:* Original. *Top right:* Blurred Goldhill by kernel with $STD = 3$ and corrupted by noise with $STD = 2$, $PSNR = 25.08$. *Bottom left:* Restored by SRA, $PSNR = 27$. *Bottom right:* Restored by BBA, $PSNR = 27.36$. Spline wavelet packets of fourth order from 2 scales were used



Table 7 PSNR values for the restored Goldhill image from blurred (Gaussian kernel, $STD = 2$) and noised input

STD(noise)/PSNR	1/26.59	3/26.36	5/25.93	10/24.32	50/13.94
SRA	29.23	28.19	27.61	26.76	24.34
BBA	29.47	28.57	28.07	27.12	24.57
Spline order/scale	10/2	10/2	4/2	6/3	6/4

Table 7 presents the PSNR results for the experiments where blurring was constant (convolution with Gaussian kernel, $STD = 2$) while the STD of noise varied.

In all the experiments, BBA produces higher PSNR values in comparison to SRA. Visually, it provides better resolution of the image details. Figure 12 displays the restored Goldhill from input that was blurred by a kernel with $STD = 2$ and corrupted by strong Gaussian noise with $STD = 50$.

We observe that, set aside the higher PSNR, the Goldhill restored by BBA is cleaner and sharper in comparison to the restored Goldhill by SRA.

Lena noised deconvolution: Lena, which was blurred by convolution with different Gaussian kernels and was corrupted by noise with constant $STD = 2$, was restored. Table 8 presents the PSNR results where a Gaussian noise was constant with $STD = 2$ while blurring varied.

Table 8 PSNR values for the restored Lena image from noised ($STD = 2$) and blurred with variable Gaussian kernels

STD(kernel)/PSNR	1/29.82	2/27.32	3/25.56	4/24.31	5/23.36
SRA	34.13	30.25	28.25	27	26.01
BBA	34.85	30.8	28.61	27.26	26.33
Spline order/scale	4/1	4/2	4/2	10/3	6/3

In all the experiments, BBA produces higher PSNR values in comparison to SRA. Visually, it provides better resolution of the image details. Figure 13 displays the restored Lena from an input that was blurred by a kernel with $STD = 3$ and corrupted by Gaussian noise with $STD = 2$. We observe that, set aside higher PSNR, the BBA better restored texture (hat, for example) in comparison to the performance of SRA.

Table 9 presents the PSNR results from the experiments where blurring was constant (convolution with Gaussian kernel, $STD = 2$) while the STD of the noise varied.

In all the experiments, BBA produces higher PSNR values in comparison to the performance of SRA. Visually, it provides better resolution of the image details. Figure 14 displays the restored Lena from the input that was blurred by kernel with $STD = 2$ and corrupted by strong Gaussian noise with $STD = 50$.

Fig. 12 Goldhill. *Top left:* Original. *Top right:* Blurred Goldhill by kernel with $STD = 2$ that was buried in noise with $STD = 50$, $PSNR = 13.94$. *Bottom left:* Restored Goldhill by SRA, $PSNR = 24.34$. *Bottom right:* Restored Goldhill by BBA, $PSNR = 24.57$. Spline wavelet packets of sixth order from 4 scales were used



Table 9 PSNR values for the restored Lena image from blurred (Gaussian kernel, $STD = 2$) and noised input

STD(noise)/PSNR	1/27.43	3/29.15	5/26.63	10/24.79	50/13.98
SRA	31.14	29.70	28.97	27.88	24.72
BBA	31.62	30.39	29.52	28.29	25.14
Spline order/scale	12/2	4/2	4/2	6/3	4/4

We observe that, set aside the higher PSNR, the BBA-restored Lena is sharper in comparison to the restored Lena by SRA.

7.4 Restoration of the Severely Damaged *Fingerprint* Image

The BBA proved to be successful in the restoration of images, which were severely damaged either by blurring or by noise or by both. We illustrate this claim by restoring *Fingerprint* image. Figure 15 displays the original image and three images that were damaged by different causes.

We observe that in all the damaged fingerprints the structure of the fingerprint is almost indistinguishable. Figure 16 displays the results of the reconstruction of the damaged images. Left figures show the reconstruction by SRA while the right figures show the reconstruction by BBA. The sin-

gle bottom figure displays the restored fingerprint by BPA. The PSNR values for the BBA-restored exceed those of the SRA-restored ones and their visual quality is incomparably better. The BPA-restored C10 image is advantageous over the BBA one.

8 Conclusions

We presented a block based algorithm (BBA) that provides a stable approximated solution to recover signals and images that are blurred and noised. The solution is provided by a spline function, which is a linear combination of orthonormal wavelet packets that are related to different resolution scales and frequency bands. The introduction of diversity of spline wavelet packets enables to have flexible adaptation of the algorithm to the available data satisfying desirable properties of the solution. The adaptation is achieved automatically. The only a priori information needed is noise estimation, which is discussed in Sect. 5.1.4. The Spline Harmonic Analysis technique, which perfectly fits to convolution problems, enables to have an explicit construction of a diverse library of spline wavelet packets and yields powerful tools for fast implementation of the algorithm.

Fig. 13 Lena. *Top left:* Original; *Top right:* Blurred Lena by a kernel with $STD = 3$ and corrupted by noise with $STD = 2$, $PSNR = 25.56$. *Bottom left:* Restored Lena by SRA, $PSNR = 28.25$. *Bottom right:* Restored Lena by BBA, $PSNR = 28.61$. Spline wavelet packets of the fourth order from 2 scales were used



The basic idea of the method is to implement the regularized deconvolution of signals (images) separately in different frequency bands by assuming that the relative portions of the coherent signal and noise are different in different frequency bands. Representation of a signal (image) in a variety of frequency bands is achieved by its expansion with orthonormal bases formed from translations of the spline wavelet packets. The spectra of these wavelet packets are close to rectangular and form a variety of splits of the signal's frequency domain. An optimal split is achieved by using the Best Basis scheme (BBA). Additional adaptation abilities stem from varying orders of the involved splines and the depths of the decomposition. Another adaptation scheme is implemented via the so-called Block Pursuit algorithm (BPA), which, to some extent, is related to the Matching Pursuit method.

The conducted experiments prove the efficiency of the algorithm for solving the general problem of deconvolved noised signals (images). In addition, it was even efficient in the two extreme cases: 1. Denoising of the object, which was not convolved. 2. Deconvolution of an object when noise is not present. Since the presented methods extend the classical Tikhonov regularization method, we compared their performance with the performance of the standard regularized deconvolution method (SRA) (implemented by the Matlab

function `deconvreg`). In all the experiments, the BBA produced better visual quality and higher PSNR in comparison to SRA performance. The advantage of the BBA was overwhelming in the pure deconvolution experiments and in the experiments on the reconstruction of severely damaged images. However, in this latter experiments, BPA produced better results than BBA. It was achieved at the expense of much heavier computational load. While the processing of a 512×512 image by BBA requires from a fraction to a couple of seconds (depending on the kernel's passband and the depth of decomposition), BPA processing on the other hand took minutes.

We tested the dependency of the results on the splines orders and on the decomposition depth. In most deconvolution experiments, the best results were achieved by using of cubic splines (fourth order), which was not the case in the denoising experiments. A theoretical investigation is needed to explain these phenomena. In our opinion, the reason is the structure of the spectra of the wavelet packets (see Figs. 1–4). In the pure deconvolution experiments, BBA achieved the best results by using the wavelet packets from one or two finest resolution scales, while BPA involved three to five scales. BBA did the same in the experiments when noise was present.

Fig. 14 Lena. *Top left:* Original. *Top right:* Blurred Lena by kernel with $STD = 2$ that was buried in noise with $STD = 10$, $PSNR = 24.79$. *Bottom left:* Restored Lena by SRA, $PSNR = 27.88$. *Bottom right:* Restored Lena by BBA, $PSNR = 28.29$. Spline wavelet packets of the fourth order from 4 scales were used



Fig. 15 Fingerprint. *Top left:* Original. *Top right:* The affected fingerprint image by adding Gaussian noise with $STD = 200$, $PSNR = 2.1$ (N200). *Bottom left:* The fingerprint was convolved with a Gaussian kernel with $STD = 10$, $PSNR = 15.71$ (C10). *Bottom right:* The fingerprint was convolved with a Gaussian kernel with $STD = 2$ and affected by Gaussian noise with $STD = 100$, $PSNR = 7.87$ (C2N100)

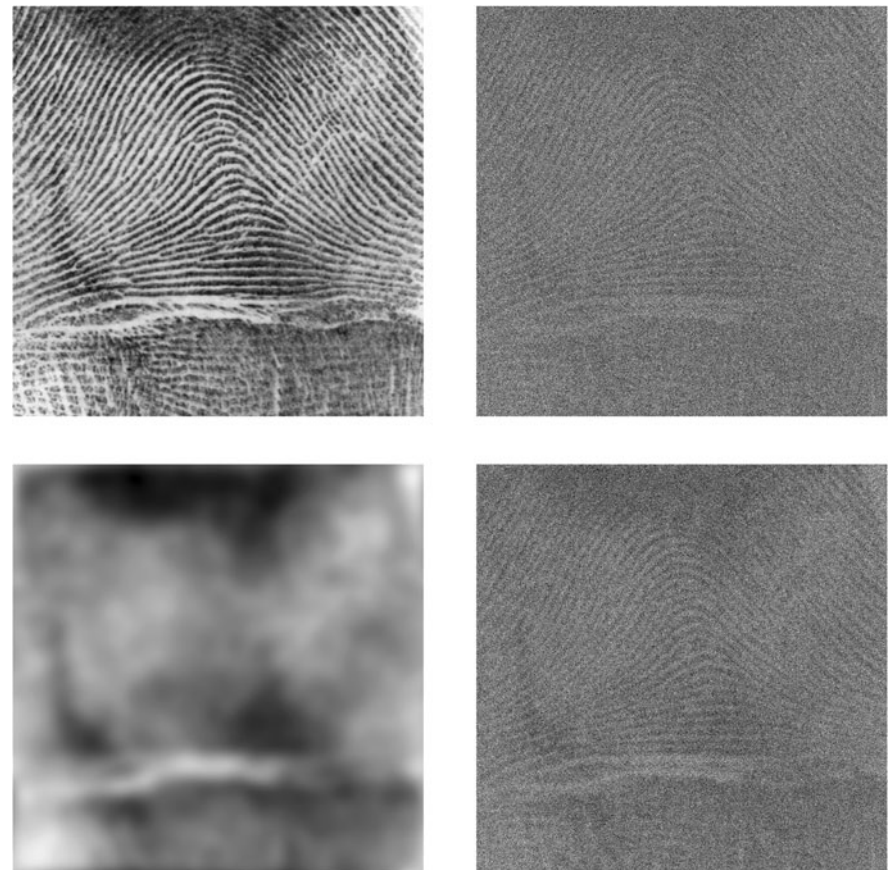
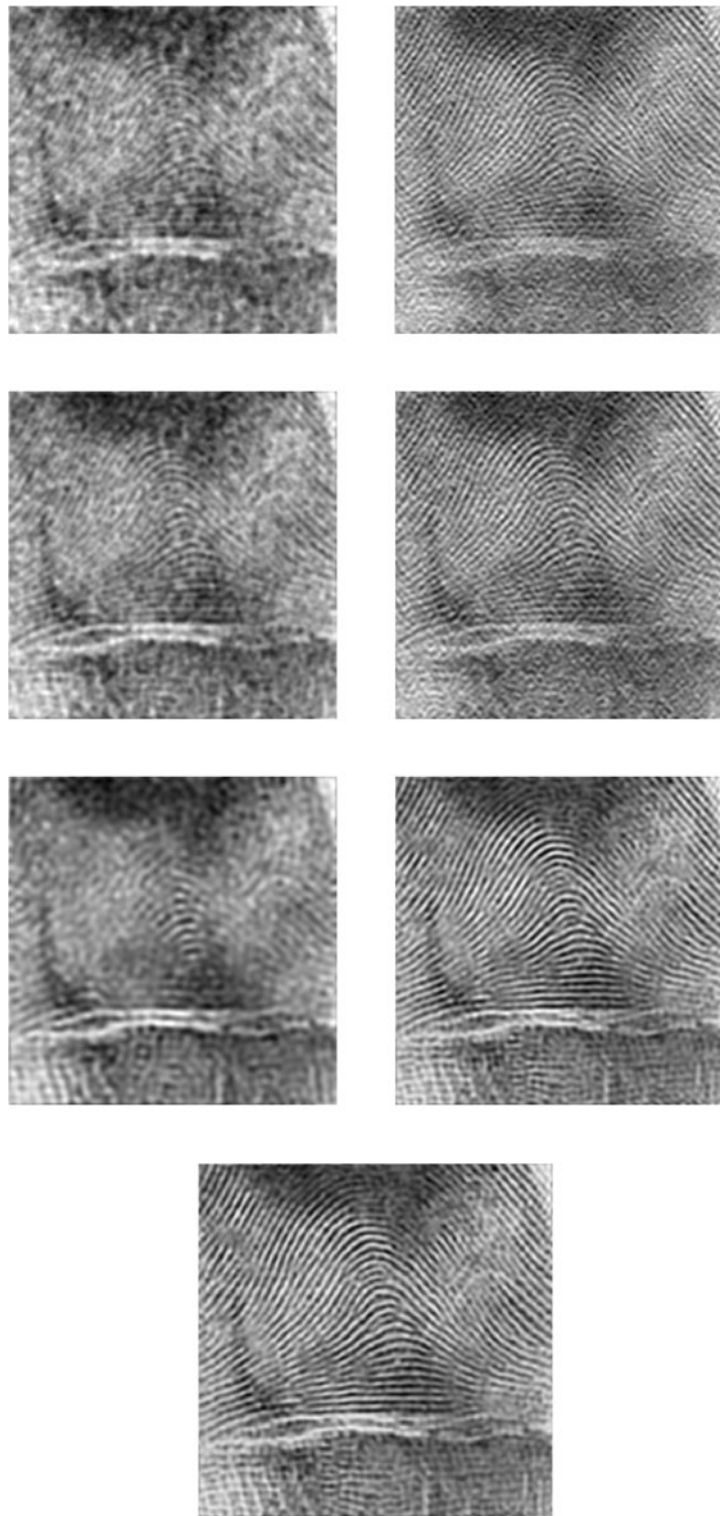


Fig. 16 Fingerprint. *Top:* Restoration from the input N200. *Left:* SRA, PSNR = 16.42. *Right:* BBA, PSNR = 17.84. *Second from top:* Restoration from the input C2N100. *Left:* SRA, PSNR = 17.06. *Right:* BBA, PSNR = 18.48. *Second from bottom:* Restoration from the input C10. *Left:* SRA, PSNR = 16.53. *Right:* BBA, PSNR = 20.25. *Bottom:* BPA, PSNR = 21.6



The designed library of spline wavelet packets supplied with an efficient implementation scheme can serve as a tool in many other applied problems where an adaptive split of the frequency domain is needed. One of such application is acoustic pattern recognition [3, 4].

References

1. Averbuch, A., Zheludev, V.: Construction of biorthogonal discrete wavelet transforms using interpolatory splines. *Appl. Comput. Harmon. Anal.* **12**, 25–56 (2002)
2. Averbuch, A., Zheludev, V.: Spline-based deconvolution. *Signal Process.* **89**, 1782–1797 (2009)

3. Averbuch, A.Z., Hulata, E., Zheludev, V.A., Kozlov, I.: A wavelet packet algorithm for classification and detection of moving vehicles. *Multidimens. Syst. Signal Process.* **12**(1), 9–31 (2001)
4. Averbuch, A., Zheludev, V., Rabin, N., Schclar, A.: Wavelet based acoustic detection of moving vehicles. *Multidimens. Syst. Signal Process.* **20**, 55–80 (2009)
5. Battle, G.: A block spin construction of ondelettes. Part I. Lemarié functions. *Commun. Math. Phys.* **110**, 601–615 (1987)
6. Charles, C., Leclerc, G., Louette, P., Rasson, J.-P., Pireaux, J.-J.: Noise filtering and deconvolution of XPS data by wavelets and Fourier transform. *Surf. Interface Anal.* **36**, 71–80 (2004)
7. Donoho, D.L.: Nonlinear solution of linear inverse problems by wavelet-vaguelette decomposition. *Appl. Comput. Harmon. Anal.* **2**, 101–126 (1995)
8. Coifman, R.R., Meyer, Y., Wickerhauser, M.V.: Adapted waveform analysis, wavelet-packets, and applications. In: *Proceedings of ICIAM'91*, pp. 41–50. SIAM Press, Philadelphia (1992)
9. Coifman, R.R., Wickerhauser, M.V.: Entropy-based algorithms for best basis selection. *IEEE Trans. Inform. Theory* **38**(2), 713–718 (1992)
10. De Mol, C., Defrise, M.: A note on wavelet-based inversion methods. Inverse problems, image analysis and medical imaging. *Contemp. Math.* **313**, 85–96 (2002)
11. Daubechies, I., Defrise, M., De Mol, C.: An iterative thresholding algorithm for linear inverse problems with a sparsity constraint. *Commun. Pure Appl. Math.* **57**(11), 1413–1457 (2004)
12. Figueiredo, M.A.T., Nowak, R.D.: An EM algorithm for wavelet-based image restoration. *IEEE Trans. Image Process.* **12**(8), 906–916 (2003)
13. Donoho, D., Johnstone, I.: Ideal spatial adaptation via wavelet shrinkage. *Biometrika* **81**, 425–455 (1994)
14. Fan, J., Koo, J.-Y.: Wavelet deconvolution. *IEEE Trans. Inform. Theory* **48**(3), 734–747 (2002)
15. Janssen, A.J.E.M.: The Zak transform: a signal transform for sampled time-continuous signals. *Philips J. Res.* **43**, 23–69 (1988)
16. Lattès, R., Lions, J.-L.: *Méthode de quasi-réversibilité et applications*. Dunod, Paris (1967)
17. Lemarié, P.G.: Ondelettes à localisation exponentielle. *J. Math. Pure Appl.* **67**, 227–236 (1988)
18. Mallat, S., Zhang, Z.: Matching pursuit with time-frequency dictionaries. *IEEE Trans. Signal Process.* **41**(12), 3397–3415 (1993)
19. Neelamani, R., Choi, H., Baraniuk, R.: ForWaRD: Fourier-waveletregularized deconvolution for ill-conditioned systems. *IEEE Trans. Signal Process.* **52**(2), 418–433 (2004)
20. Philips, D.L.: A technique for the numerical solution of certain integral equations of the first kind. *J. Assoc. Comput. Mach.* **9**(1), 84–97 (1962)
21. Schoenberg, I.J.: *Cardinal Spline Interpolation*. CBMS, vol. 12. SIAM, Philadelphia (1973)
22. Tikhonov, A.N.: Solution of incorrectly formulated problems and the regularization method. *Sov. Math., Dokl.* **4**, 1035 (1963)
23. Tikhonov, A.N., Arsenin, V.Y.: *Solution of Ill-posed Problems*. Wiley, New York (1977)
24. Vonesch, C., Unser, M.: A fast thresholded Landweber algorithm for wavelet-regularized multidimensional deconvolution. *IEEE Trans. Image Process.* **17**(4), 539–549 (2008)
25. Wahba, G.: *Spline Models for Observational Data*. SIAM, Philadelphia (1990)
26. Wickerhauser, W.V.: *Adapted Wavelet Analysis from Theory to Software*. AK Peters, Wellesley (1994)
27. Wiener, N.: *Extrapolation, Interpolation and Smoothing of Stationary Time Series with Engineering Applications*. Wiley, New York (1949)
28. Zak, J.: Finite translations in solid-state physics. *Phys. Rev. Lett.* **19**(4), 1385–1387 (1967)
29. Zheludev, V.A.: An operational calculus connected with periodic splines. *Sov. Math., Dokl.* **42**, 162–167 (1991)
30. Zheludev, V.A.: Periodic splines and the fast Fourier transform. *Comput. Math. Math. Phys.* **32**, 149–165 (1991)
31. Zheludev, V.A.: Spline-operational calculus and inverse problem for heat equation. In: Szabados, J., Tandoi, K. (eds.) *Proc. Int. Conf. Approximation Theory, Kecskemét, Hungary, 1990*. *Colloq. Math. Soc. J. Bolyai*, vol. 58, pp. 763–783. Elsevier, Amsterdam (1991)
32. Zheludev, V.A.: Periodic splines, harmonic analysis, and wavelets. In: Zeevi, Y.Y., Coifman, R. (eds.) *Signal and Image Representation in Combined Spaces*. *Wavelet Anal. Appl.*, vol. 7, pp. 477–509. Academic Press, San Diego (1998)
33. Zheludev, V.A.: Integral representation of slowly growing equidistant splines. *Approx. Theory Appl.* **14**(4), 66–88 (1998)
34. Zheludev, V.A.: Wavelet analysis in spaces of slowly growing splines via integral representation. *Real Anal. Exch.* **24**, 229–261 (1998/99)
35. Zheludev, V.A.: Interpolatory subdivision schemes with infinite masks originated from splines. *Adv. Comput. Math.* **25**, 475–506 (2006)
36. Zheludev, V.A., Averbuch, A.Z.: Computation of interpolatory splines via triadic subdivision. *Adv. Comput. Math.* **32**(1), 63–72 (2010)